



저작자표시-비영리-변경금지 2.0 대한민국

이용자는 아래의 조건을 따르는 경우에 한하여 자유롭게

- 이 저작물을 복제, 배포, 전송, 전시, 공연 및 방송할 수 있습니다.

다음과 같은 조건을 따라야 합니다:



저작자표시. 귀하는 원저작자를 표시하여야 합니다.



비영리. 귀하는 이 저작물을 영리 목적으로 이용할 수 없습니다.



변경금지. 귀하는 이 저작물을 개작, 변형 또는 가공할 수 없습니다.

- 귀하는, 이 저작물의 재이용이나 배포의 경우, 이 저작물에 적용된 이용허락조건을 명확하게 나타내어야 합니다.
- 저작권자로부터 별도의 허가를 받으면 이러한 조건들은 적용되지 않습니다.

저작권법에 따른 이용자의 권리는 위의 내용에 의하여 영향을 받지 않습니다.

이것은 [이용허락규약\(Legal Code\)](#)을 이해하기 쉽게 요약한 것입니다.

[Disclaimer](#)

**EVALUATE OF THE ION BEAM BEHAVIOR OF RADIO-
FREQUENCY ION THRUSTER**

울산대학교 대학원

기계공학과 항공우주공학전공

NGUYEN THI THU HUONG

EVALUATE OF THE ION BEAM BEHAVIOR OF RADIO-FREQUENCY ION THRUSTER

A thesis submitted in partial fulfillment of the requirement for the Degree of
Master of Science to the Department of Aerospace Engineering, University of Ulsan, Korea

By

NGUYEN THI THU HUONG

JUNE 2021

**EVALUATE OF THE ION BEAM BEHAVIOR OF
RADIO-FREQUENCY ION THRUSTER**

**This certifies that the dissertation of
NGUYEN THI THU HUONG is approved by**

Committee Chairman: Assist. Prof. Choi, Sang-Jo



.....

Committee Member: Prof. Shin Jichul



.....

Committee Member: Assist. Prof. Yoon Ho Lee



.....

Department of Aerospace Engineering

University of Ulsan, Korea

JUNE 2021

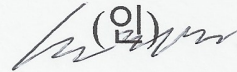
NGUYEN THI THU HUONG 의

공학석사학위논문을인준함

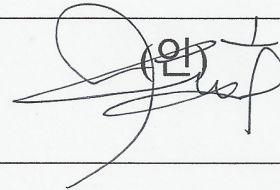
심사위원장 최 상 조

 (인)

심사위원 신지철

 (인)

심사위원 이윤호

 (인)

울산대학교대학원

기계공학과 항공우주공학전공

2021년 6월

Acknowledgements

Firstly, I would like to thank my thesis advisor, professor Shin Jichul at University of Ulsan. The door to Prof. Shin office was always open whenever I ran into a trouble spot or had a question about my research or writing. All of my work presented in this thesis would not have been possible without your support.

I would also like to thank the experts who were involved in the validation survey for this thesis: Assist. Prof. Choi Sang-Jo, and Assist. Prof. Yoonho Lee. Without their passionate participation and input, the validation survey could not have been successfully conducted.

Finally, I must express my very profound gratitude to my parents and to my friends for providing me with unfailing support and continuous encouragement throughout my years of study and through the process of researching and writing this thesis. I would not have been able to achieve this accomplishment without them.

Ulsan, June 2021

Nguyen Thi Thu Huong

Content

Acknowledgements.....	5
LIST OF FIGURES	8
LIST OF TABLES.....	11
Abstract.....	12
Chapter 1. Introduction	12
1.1 Introduction about development history of electric propulsion.....	12
1.2 Introduction to micro ion engine.....	14
1.3 Scope of dissertation	15
1.4 Limitation of dissertation.....	16
1.5 Dissertation outline	16
Chapter 2. Theory fundamentals of Radio-Frequency ion thruster	17
2.1 Fundamental description of Radio-frequency ion thruster	17
2.2 Advantages and disadvantages	19
2.3 Summary.....	20
Chapter 3. The theoretical analysis Tool Development (AARL model)	20
3.1 Introduction.....	20
3.2 Description of the model.....	21
3.3 Plasma discharge in RF ion thruster	24
3.3.1 Neutral gas model	24
3.3.2 Particle and power balance	26

3.3.3 Electromagnetic model of RF ion thruster.....	28
3.4 Model and result	31
3.5 Summary	36
Chapter 4. Measurement system	37
4.1 Faraday probe.....	37
4.1.1 Formation of Faraday probe.....	37
4.1.2 Design Faraday probe for RF thruster.	38
4.1.3 Travel system	40
4.2 RPA probe.....	42
4.2.1 Formation of RPA probe.....	42
4.2.2 Design RPA probe:	44
4.3 Development of Torsional Thrust Stand.....	45
4.3.1 Torsion balance dynamics.....	46
4.3.2 PCB electronic comb	47
4.4 Summary	52
Chapter 5. Simulation and experiment.....	52
5.1 Simulation and experimental equipment	52
5.2 Experiment and analysis for Faraday probe.....	56
5.3 Experiment and analysis for RPA probe.....	59
5.4 Calibration of Torsional Thrust Stand	62
5.5 Calibration of DC-powered Electrostatic Fin	63

5.6 Summary	65
Chapter 6. Conclusion and Future Work	66
6.1 Conclusion	66
6.2 Future work.....	67
REFERENCES	67

LIST OF FIGURES

Fig. 1.1 Number of EP-based GEO satellites launched in the years 1993-2016 (3-year running average), divided into electric thruster subclasses[10]	14
Fig. 1.2 Comparison between Micro Plasma Thrusters.....	14
Fig. 1.3 Outline of chapters	17
Fig. 2.1 Structure of RF ion thruster.....	18
Fig. 3.1 Schematic of an RIT 10.....	21
Fig. 3.2 Flow chart of the analytical discharge of AARL model	23
Fig. 3.3 The interface of Theoretical Analysis Tool Development	31
Fig. 3.4 Comparing the calculations obtained from the models with the experimental results of ESA-XX at 780 A	32
Fig. 3.5 The ion production cost channels map of the ESA-XX RF ion thruster at $I_b=0.78$ A obtained by our analytical model.....	33
Fig. 3.6 Comparing the calculations obtained from the models with the experimental results of ESA-XX at $I_b= 2$ A	34
Fig. 3.7 Comparing the calculations obtained from the models with the experimental results of RIM-4 at $I_b= 10$ mA and 12,5mA	34

Fig. 3.8 Comparing the calculations obtained from the models with the experimental results of RIM-4 at $I_b = 7.5\text{mA}$	35
Fig. 3.9 Efficiency for various area ratio.	36
Fig. 4.1 The schematic of the Faraday probe.....	37
Fig. 4.2 Faraday probe of ARRL lab	39
Fig. 4.3 the location of the Faraday probe[24]	40
Fig. 4.4 Travel system for Faraday probe : near field (left), far field (right)	40
Fig. 4.5 remote control of step motor	41
Fig. 4.6 Travel system in chamber.....	42
Fig. 4.7 Control circuit.....	42
Fig. 4.8 Example for electric circuit of RPA probe	44
Fig. 4.9 Shape drawing of the thrust stand installed inside the vacuum chamber	46
Fig. 4.10 Relationship between electric field and electric potential.....	48
Fig. 4.11 Simple AARL fin comb circuit	49
Fig. 4.12 : Layout of the polar plate	49
Fig. 4.13 Electric potential and electric field.....	50
Fig. 4.14 Shape the polar plates.....	51
Fig. 4.15 The graph represents the relationship of Δz and electromagnetic force at $V_0 = 1000\text{V}$	51
Fig. 5.1 : Simulation geometry model	52
Fig. 5.2 : Method of obtaining ion beam profiles [41]	54
.....	55
Fig. 5.3 Simulation PIC when there is a shell (lower) and b) in absence of a shell (upper)	55
Fig. 5.4 Comparison between electric field (cover) and electric field (no cover) at $z = 2.5\text{mm}$	56

Fig. 5.5 Comparing divergence angle between in case engine have cover and no cover.....	56
Fig. 5.6 : Experimental images in a vacuum chamber.....	57
Fig. 5.7 : Result experiment when change RF power.....	58
Fig. 5.8 Result experiment when change mass flow rate	58
Fig. 5.9 Result experiment when change RF power (set radial coordinate).....	59
Fig. 5.10 Experimental images in a vacuum chamber.....	60
Fig. 5.11 Result experiment of RPA probe.....	61
Fig. 5.12 RPA I-V and dI/dV curve from measurements 100 mm at $r = 0$	61
Fig. 5.13 Experiment Torsional Thrust Stand	62
Fig. 5.14 Compare displacement measurement.....	63
Fig. 5.15 Experiment DC- Electrostatic Fin	64
Fig. 5.16 Comparision of force measument.....	65

LIST OF TABLES

Table 2.1 : Examples of Small Scale RF Ion Engines 18

Table 4.1 Manufacturing paraments of Faraday probe39

Table 4.2 Manufacturing parameters of RPA probe45

Table 5.1 Parameters in experiment of Faraday probe.....57

Table 5.2 Parameters in experiment of RPA probe.....59

Abstract

Today, the application of satellite spatial propulsion using the practice of electric propulsion is quite common, including the success of the development of the hall and ion thruster. In 1884, Hittorf introduced for the first time a Radio Frequency Ion Thruster (RIT), which produced a plasma in a vacuum using a magnetic field. Inheriting his ideas and from the achievements of Applied Aerodynamics Research Laboratory, we study theoretical analysis Tool Development and measurement system. The system under research and development includes faraday probe, RPA probe and Torsional Thrust Stand with ion thruster and was tested with different input locations and conditions to evaluate the ion current density and ion energy distribution. The specifications of Faraday probe and RPA probe are designed based on the electronic density and temperature analysis, etc.

Chapter 1. Introduction

1.1 Introduction about development history of electric propulsion

Coined in the early half of the 20th century, the idea of electronic propulsion has been developed by researchers around the world and widely applied in technologies such as Hall thruster and ion engine [1-3]. Over the years of development, plasma propulsion has been used in a number of scientific missions such as proving the ion engine measurement concept (SERT-NASA), being included in the propulsion engine for the Soviet probe Zond 2, and applied in the flyby orbiting around comets and asteroids (Deep Space 1-NASA), “raise its orbit from medium Earth orbit (MEO) to the geostationary orbit” (ESA) [4]. EP technologies have been developed in some countries, including the United States, the Former Soviet Union, and Japan.

Electric propulsion was first utilized in 1964 by NASA and the Soviet Union. In 1968 US LES and NOVA satellites used pulsed plasma propulsion engine to achieve a "drag-free" orbit [5-6]. In 1981, the use of electric propulsion for commercial purposes was firstly marked with the launch of GEO Intelsat V series of satellites, followed by continued successes of RCA Satcom 1 with 77 ships and about 20 geographically asynchronous satellites in the original Iridium constellation [7-8]. Due to the efficiency improvement properties provided by electromechanical motors, the use of pulsed plasma thruster or resist jets cannot be applied instead.

As EP technology was widely adopted around the world, in 1993, Telstar 401 telecom satellites were successfully launched using arcjet thrusters for GEO orbit [9]. The relationship between the choice of propulsion technology and launcher requirements is best demonstrated through the selection of arcjets for North south station keeping, for example, the mass reduction enabled by arcjets helps to save costs in launching. The success of Telstar 401 marks a turning point in removing barriers, helping private satellite operators develop EP technology.

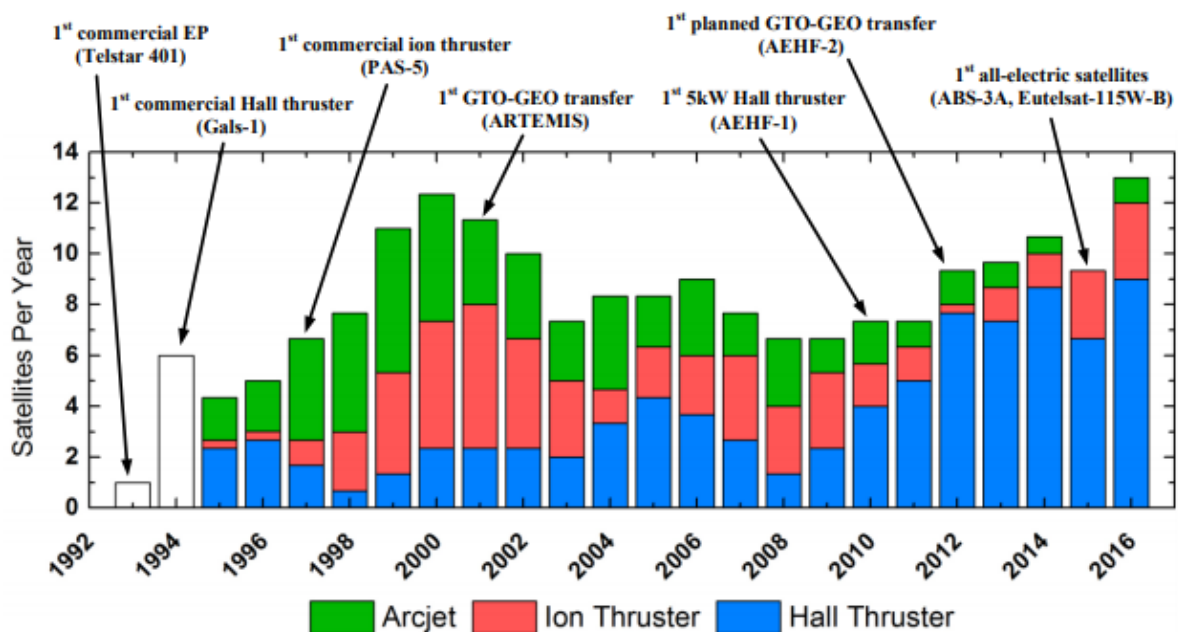


Fig. 1.1 *Number of EP-based GEO satellites launched in the years 1993-2016 (3-year running average), divided into electric thruster subclasses[10]*

Following the success of the Telstar 401, the rapid increase in the number of satellite integrators deployed EP push systems is shown in Fig 1.1. From 1992 to 2000, the number of launched satellites increased continuously to 12 satellites in 2000. From 2000 to 2016 the number of launched satellites increased, sometimes decreased, but always maintained around at least 7 satellites in this period, electric propulsion with additional primes adopted like gridded ion and Hall-effect thrusters gradually replaced the arcjet technology. The number of satellites using arcjet technology decreased from 4 to 1 from 2000 to 2016. EP technology is demonstrated to perform many different functions of and is increasingly popular in most space applications, from CubeSats, "via Earth observation satellites at LEO, to remote interplanetary missions" [11]. The first RIT Ion Thruster with an ionic diameter of 4 to 35 cm was successfully developed at the Physikalisches Institute in Justus-Liebig-Universität Gießen in the 1960s. Based on this research, Eureka and Artemis put the RIT ion thruster to use in 2001.

1.2 Introduction to micro ion engine

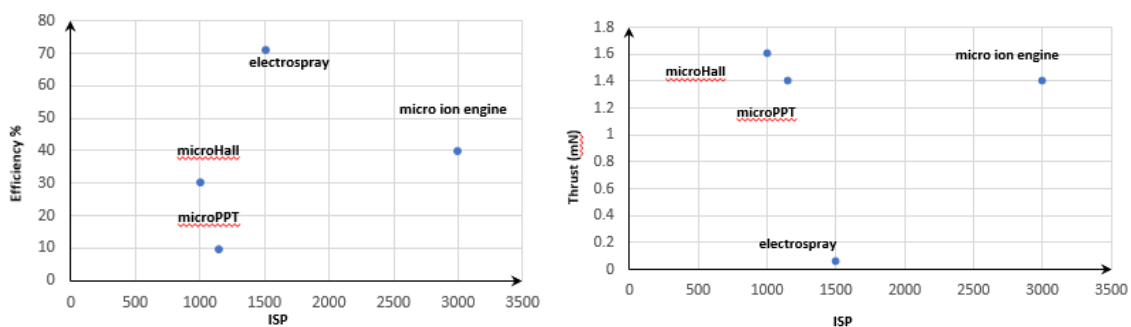


Fig. 1.2 *Comparison between Micro Plasma Thrusters*

Electrostatic propellants accelerate ionization repellents in four main categories: Field Emission Electric Propulsion (FEED), Colloid Thruster, Ion thruster, Hall Effect Thruster (HET). In particular, micro engine with small capacity, as in this study, with RF power of about

50 W, will have priority points compared to other types of motors such as: high discharge speed, high efficiency, gas promote inert, high promoting properties. According to Fig 1.2, electro spray has the most efficiency. Beside that micro ion engine has high thrust and high ISP comparing to the micro-Hall, electro spray, micro PPT [12]. However micro ion engine has drawback such as: negative power processing, grid and cathode lifetime issues, high voltage.

1.3 Scope of dissertation

The thesis focuses on the theoretical analysis of Tool Development, the development of measurement system, and along with that, some physical analysis of plasma of the RF discharge chamber was performed. The specific thesis in this dissertation are as follows:

Firstly, the performance of the RF ion thruster depends on the characteristics of the RF discharge. Therefore, for the convenience of performance analysis and calculation, we have developed a theoretical analysis tool based on RF discharge analysis. The theoretical analysis tool is developed based on the GUI to make it more intuitive and convenient. Then the design parameters are set and executed, the calculation result is saved as a data file in Excel format.

Secondly, a measurement system was developed for Radio-Frequency ion thruster(50W) which made by Applied Aerodynamics Research Laboratory in University of Ulsan. The system includes: Faraday probe, RPA probe and Torsional Thrust Stand. The RPA cup and Faraday probe design parameters rely on expected range of ion current density and temperature, the sheath thickness. Evaluations of the designed faraday probe and RPA probe system in experimental in vacuum chamber and calibration testing of thrust stand to be tested. Besides, simulation of electromagnetic force measurement system used for 50 W class RF gridded ion thruster was performed.

Finally, Analysis plasma physic of RF discharge chamber: electron density, electric potential distribution, electron temperature distribution of plasma in RF discharge chamber.

1.4 Limitation of dissertation

The design and manufacturing methods and evaluate the ion current density of Radio-Frequency ion thruster are presented this study. Theoretical analysis Tool Development was developed in order design the small -scale thruster based on RF discharge analysis. Along with that are the current ion density estimates by a system of faraday probe and RPA probe in a vacuum chamber. However, some limitations in the thesis are as follows:

- Due to experimental limitations, verification cannot be performed between analytical model and experimental data of thruster ions. However, the analytical results are verified by experimental results from the references.
- Torsional Thrust Stand was not experimented in the vacuum chamber

1.5 Dissertation outline

The theoretical analysis tool and measurement system are builded at AARL lab, University of Ulsan. This thesis has structure illustrated by the following:

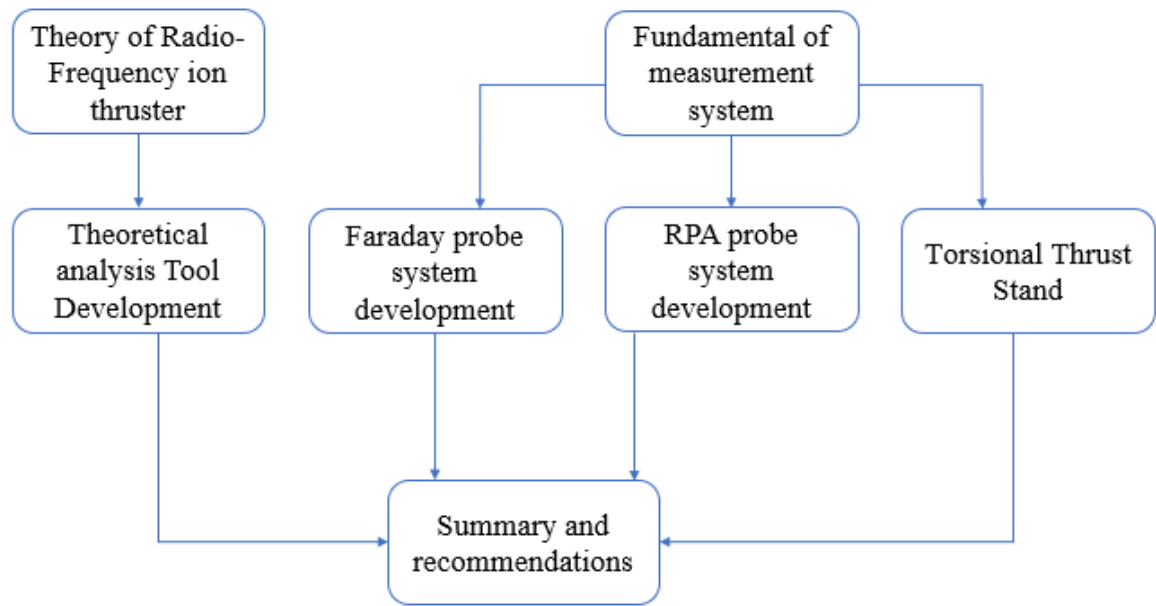


Fig. 1.3 *Outline of chapters*

Chapter 1 of this thesis is overview introduction. Chapter 2 presents about theory fundament of Radio-Frequency ion thruster. The theoretical analysis Tool Development based on RF discharge analysis are presented in chapter 3. In chapter 4, the process of forming and developing a measurement system is presented. The experimental results measured and simulated by the system of faraday probe and RPA probe are shown in Chapter 5. Chapter 6, conclusion and future development direction are presented in this chapter.

Chapter 2. Theory fundamentals of Radio-Frequency ion thruster

2.1 Fundamental description of Radio-frequency ion thruster

The previous design for thruster has some issues as potential life or power supply with ion thrusters utilize hollow cathode. Radio-Frequency ion thruster uses an inductive plasma generator to create electromagnetic field which heat particulars, ionize the injected gas, that created plasma. According to Figure 2.1, structure of Radio-Frequency ion thruster uses xenon

gas as input material. The fuel is injected into the discharge chamber, a RF coil wrapped around chamber (shape of discharge chamber can be cylindrical, conical, ...) and grid system.

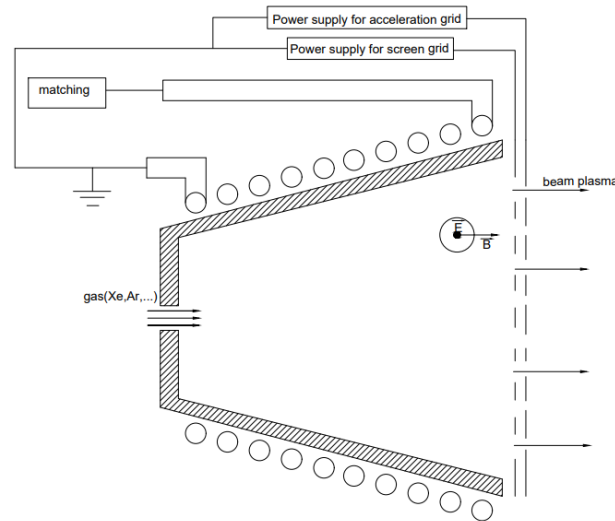


Fig. 2.1 Structure of RF ion thruster

Table 2.1 : Examples of Small Scale RF Ion Engines

	μ XRT – 2.5(JLU)	BRFIT-3 (BUSEK)	RIT μ X (ARIANESPACE)	ESA 26
THRUST	0.05-0.6 mN	1.6 mN	50-500 μ N	200 mN
POWER	34.4 W	80W	<50 W	6.2kW
ISP	2861s	>7600s	> 10kNs up to 200kNs	4500s
GRID DIAMETER	22.5mm	30mm	76mm	26 mm

The previous design for thruster to have some issues as potential life or power supply with ion thrusters utilize hollow cathode. Radio-Frequency ion thruster uses an inductive plasma

generator to create electromagnetic field which heat particulars, ionize the injected gas, that created plasma. According to Figure 2.1, structure of Radio-Frequency ion thruster uses xenon gas as input material. The fuel is injected into the discharge chamber, a RF coil wrapped around chamber (shape of discharge chamber can be cylindrical, conical, ...) and grid system. Advantage of family of RIT Ion thruster compare with the previous design is the discharge chamber no thermionic electron emitter so that is easy increasing the lifetime of grids. Following the figure 2.1, the RF coil wrapped around the discharge chamber distributed alternating from 1 MHz to 13.56 MHz. An RF sinusoidal current (\vec{I}_C) through the RF coil create a magnetic field axial \vec{B} in discharge chamber. According to Faraday's law electromagnetic induction, that creates an azimuthal electric field. The electrons inside discharge chamber are created by oscillation of RF current through in the coil. When electrons enough energy cause neutral propellant ionization process. Ions produced of this process which will move to boundary the wall, a screen grid. There are some successful developments of small size RF ion thrusters as shown table 1. RF ion thrusters are being developed by several institutes around the world such as Giessen University, Busek, and Arianespace. We hope to become a fast follower to these RF ion thrusters.

2.2 Advantages and disadvantages

On NASA spacecraft, thruster ions are used the most, which also proves to be a very successful and superior design. The ion thruster have the following advantages: high efficiency, high specific impulse, inert propellant, high exhaust speed. Efficiency range of ion thruster is about 40-80% higher than other engines of the same size such as Arcjet, Hall thruster, Pulsed plasma thruster. However, the extracted ion beam is limited by the electric current in the grid system, so the average repulsion density will be best. The ion thrusters also have the best significant Isp of about 8 times the same size of Resistojet and 5 times more than Arcjet [12].

In addition, they use gas propellants used such as Argon, and Xenon are less toxic than Teflon. The absence internal cathode helps to reduce the problem of erosion of the engine life should be significantly prolonged. This is an advantage in long-term missions such as holding and dragging stations in high orbit or interplanetary travel.

Despite its many advantages, RF ion engine have problems with miniaturization of amplifier components, complex design methods. Impedance matching for RF circuits has high coupling efficiency and low power loss and requires knowledge of the plasma such as previously unknown electrical properties. In addition, parasitic power loss is typical as the process of heating the coil by ohmic. Development of high-performance RF power electronics is an ongoing research area in the world but not within the scope of this thesis.

2.3 Summary

This chapter presents the basic theory of RF ion thruster and also discusses its advantages and disadvantages. The development of a computational tool for ion engine research and advancement is essential and the principles and physics of the RF ion thruster are shown in Chapter 3.

Chapter 3. The theoretical analysis Tool Development (AARL model)

3.1 Introduction

The performance of the RF ion thruster depends on the characteristics of the RF discharge. Therefore, for the convenience of performance analysis and calculation, we have developed a theoretical analysis tool based on RF discharge analysis. This model is based on a 0-D analytical model for discharge chamber. The theoretical analysis tool is developed based on the GUI to make it more intuitive and convenient than older. In addition, this new model helps to compute the effect of the grid geometry values on the system based on Clausing Factor

Monte Carlo calculation [3]. Then the design parameters are set and executed, the calculation result is saved as a data file in Excel format. Results from this tool in order to find suitable parameter geometrical during engine manufacturing. Computational modeling of RF ion thruster is used frequently in the manufacturing process, typically as Goebel model [13], that suggested a theoretical analysis Tool Development can be used to find efficient of ion thruster. This tool has a few shortcomings during considering effects such as magnetic field of RF ion thruster.

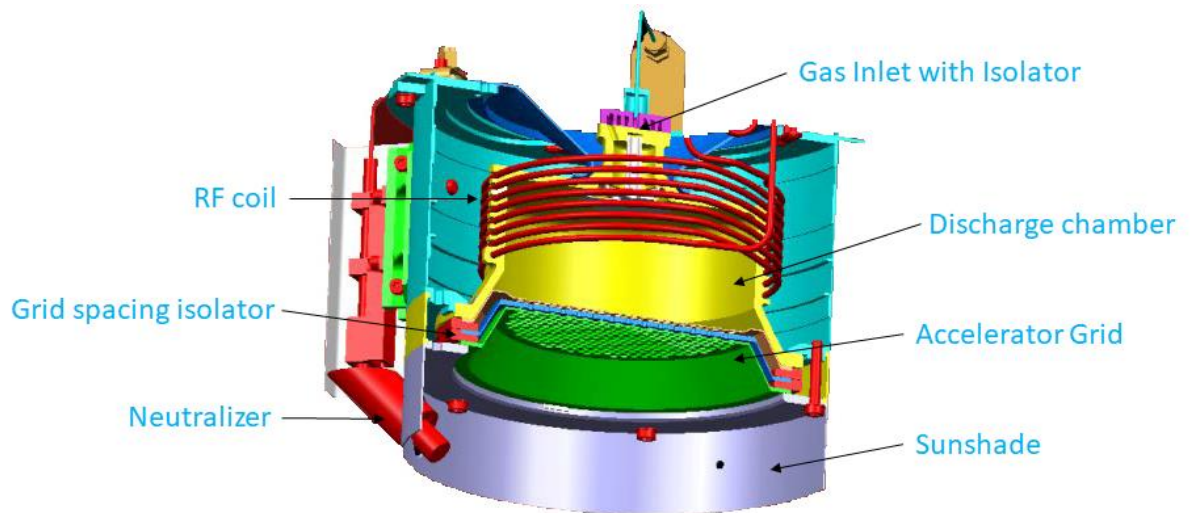


Fig. 3.1 Schematic of an RIT 10

For one real example about RF ion thruster shown Figure 3.1(RIT-XT thruster from JLU [14]. According to the figure, discharge chamber is conical made by alumina insulator, an antenna coiled wrapped around the chamber. A hollow neutralizer is used to reduce the divergence angle of the plasma beam.

3.2 Description of the model

Firstly, geometrical parameters such as volume of chamber, the wall area are determined by the following formulas:

$$V_{\text{conical}} = \frac{1}{3} \pi (r_1^2 + r_2^2 + r_1 r_2) h \quad (3.1)$$

$$A_w = \pi (r_1 + r_2) l + \pi r_2^2 \quad (3.2)$$

$$A_s = \frac{\pi r_b^2}{4} \quad (3.3)$$

Total ion loss area follow this equation:

$$A_t = A_g + f_c \times A_w + A_{bw} \quad (3.4)$$

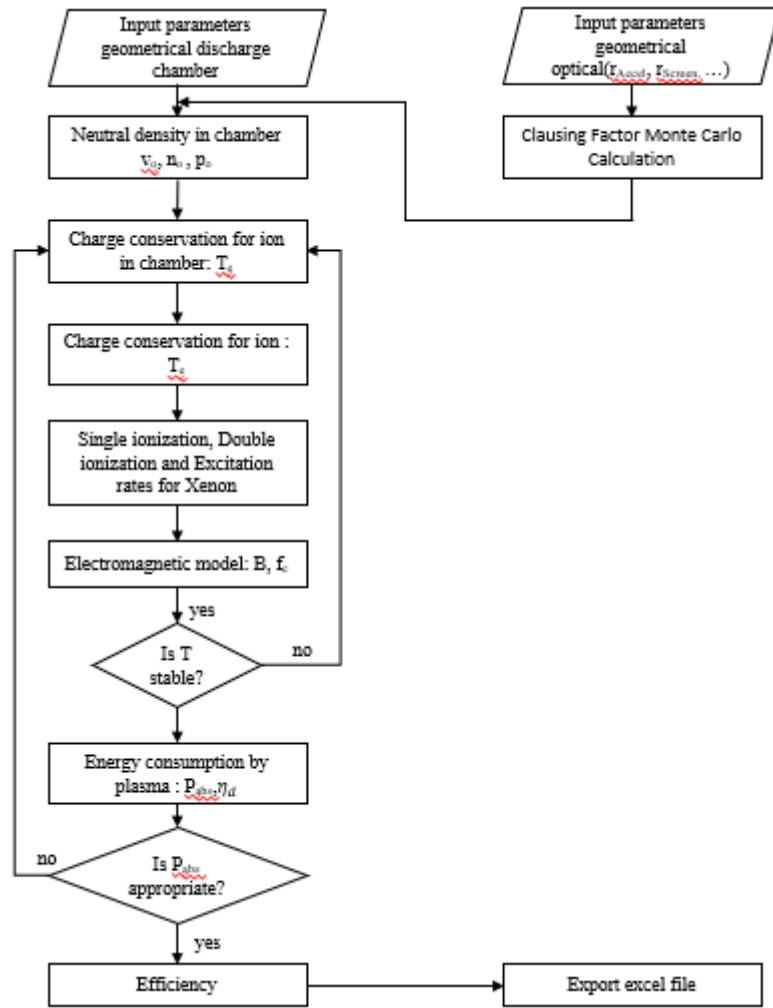


Fig. 3.2 Flow chart of the analytical discharge of AARL model

In fact, Plasma is always in a nearly neutral state [15], so the ionic density calculated approximately equal to the electron density ($n_i \approx n_e$). The power loss in the RF ion thruster is mainly due to free electrons and ions entering the wall, the plasma edge sheath potential is used to estimate this loss. The energy characteristics of the thruster still depend on the secondary electrons [3]. In the [16-18] reports, it is shown that the secondary electronic efficiency is determined by the following equation:

$$\gamma = \Gamma(2 + b)aT_{eV}^b \quad (3.5)$$

Where Γ is the gamma function, value of the coefficients a and b respectively Al_2O_3 (0.145;0.650) – Stainless steel (0.040,0.610).

3.3 Plasma discharge in RF ion thruster

3.3.1 Neutral gas model

The temperature of the electron is determined by the rate of production of single and stimulating neutral ions, so the calculation of neutral gas density is very important. The calculated parameters of the neutral gas such as the amount of ionization out of the chamber, the mesh, and the velocity are determined by the following equations:

$$Q_{out} = Q_{in} - \frac{I_B}{e} \quad (3.6)$$

$$Q_{out} = \frac{1}{4}n_0v_0A_gT_a\eta_c \quad (3.7)$$

$$v_0 = \sqrt{\frac{8k_B T}{\pi M}} \quad (3.8)$$

Beam extraction also affects the transparency of the system efficiency ion optics $T_{eff} = I_b/I_B$ [19]. The ion beam current given by:

$$I_b = \frac{1}{2}n_1eV_eA_sT_{eff} \quad (3.9)$$

In which the velocity e will be calculated as:

$$v_e = (kT_e/M)^{1/2} \quad (3.10)$$

The grid optical transparency is determined by formula:

$$T_a = \frac{1}{(1/T_s) + (1/T_{\text{accel}}) - 1} \quad (3.11)$$

$T_{\text{accel}} / T_s = 0.36$ is the conventional relation proposed by Farnell, where T_{accel} is the accelerator grid transparency.

Where A_g is open area ($A_g = \beta_{g\pi} R^2$), η_c is Clausing factor [19]. Follow these equations 3.6, 3.7, and 3.8 we have:

$$n_0 = \frac{4I_B \alpha_m}{v_0 e T_a \eta_c} \frac{1 - \frac{\eta_m}{\alpha_m}}{\eta_m} \quad (3.12)$$

The single ions and the double charged ions have been surmised that they coexist in the plasma, an equation for the propellant's use efficiency:

$$\eta_m = \dot{m}_1 / \dot{m}_p = \alpha_m (I_b M / e \dot{m}_p) \quad (3.13)$$

Where \dot{m}_p is the mass flow input to chamber of ion thruster ($\dot{m}_p = \alpha_m \frac{I_b M}{e \eta_m}$), The coefficient for a doubly charged ion given by:

$$\alpha_m = \frac{1 + \frac{1}{2} \frac{I^{++}}{I^+}}{1 + \frac{I^{++}}{I^+}} \quad (3.14)$$

The neutral pressure in the discharge chamber is calculated by the formula:

$$P_0 = 1.04 \times 10^{-25} n_0 \times T_0 [K] \quad (3.15)$$

3.3.2 Particle and power balance

In fact, the singly ionized particle and doubly particle coexist in the plasma, so we have the total flow of ionic products given by:

$$I_{\text{Total}} = I^+ + I^{++} = I_w + I_{\text{scr}} + I_b \quad (3.16)$$

This total product is also equal to the loss of ions entering the wall, the grid and the plasma through the grid system. Production rate of singly ionized and doubly ionized of the propellant (Ar, Xe, ...) is modeled by equations:

$$I^+ = n_0 n_e e \langle \sigma_i^+ v_e \rangle V_{\text{chamber}} \quad (3.17)$$

$$I^{++} = n_e^2 e \langle \sigma_i^{++} v_e \rangle V_{\text{chamber}} \quad (3.18)$$

$$I^* = \sum_j n_0 n_e e \langle \sigma_* v_e \rangle_j V \quad (3.19)$$

In which, $\langle \sigma_i^+ v_e \rangle$, $\langle \sigma_* v_e \rangle$ and $\langle \sigma_i^{++} v_e \rangle$ are single ionization rate and double ionization rate [21], respectively. Total ionic current enters the discharge chamber wall given by:

$$I_w = \frac{1}{2} n_i e \sqrt{\frac{kT_e}{M_{xe}}} A_w f_c \quad (3.20)$$

In which the confinement factor is $f_c = v_i / v_{Bohm}$. Since the RF ion thruster has a changing electric field over time that induces an induced magnetic field, it reduces the ion loss due to the ions entering the wall leading to a reduced confinement factor. The mean value of the detention factor is about 0.44 for the RF ion thruster (typical as RIT-15 engine) and possibly about 0.4 for the higher power engine [13]. In addition to the number of ions lost by penetrating the chamber wall, the amount of ions lost due to trapping by the screen mesh area, this ion flow is calculated by the equation:

$$I_{scr} = \frac{(1 - T_{eff})}{2} n_i e \sqrt{\frac{kT_e}{M_{xe}}} A_s \quad (3.21)$$

In addition to analyzing the particle equilibrium model, the study also analyzes the energy model. The absorbed power is calculated by:

$$P_{abs} = I^+ U^+ + I^{++} U^{++} + I^* U^* + (I_s + I_w + I_b)(0.5T_e + \phi) + I_a(2T_e + \phi) \quad (3.22)$$

“Where U^+ is the ionization potential, U^{++} is the second ionization potential, U^* is the average excitation potential over the excited species”[13]. The energy ϵ_i of the ions at the wall follow equation:

$$\epsilon_i = \frac{T_e}{2} + \phi \quad (3.23)$$

The power losses were caused by electron and ion given by:

$$P_{\text{ion_loss}} = (I_{\text{scr}} + I_w + I_b)(0.5T_e + \phi) \quad (3.24)$$

$$P_{\text{electron_loss}} = I_a(2T_e + \phi) \quad (3.25)$$

The loss of electrons and ions is due to the incoming flow of ions and electrons to the floating-potential walls. We have the discharge loss is:

$$\eta_{\text{d_loss}} = \frac{2n_0V}{\sqrt{\frac{kT_e}{M}} A_{\text{scr}} T_s} (\langle \sigma_i^+ v_p \rangle U^+ + \langle \sigma_i^{++} v_p \rangle U^{++}) \quad (3.26)$$

$$+ \left[\frac{(1 - T_{\text{eff}})}{2} + \frac{A_w f_c}{A_{\text{scr}} T_s} + 1 \right] (2.5T_e + 2\phi)$$

3.3.3 Electromagnetic model of RF ion thruster

A typical model of RF ion thruster would have a coil wound around the discharge chamber with N turns and RF voltage in the coil with typical frequency is in the range 1 MHz. During the cycle of the magnetic field is $1\mu\text{s}$, ions are considered to be at rest because the ion-acoustic speed at $T_e = 5\text{eV}$ is about 1.9 km / s so the ions move 2 mm. During the RF process, the electrons aren't definitely stationary, but the electrons will be held still by the ionic spatial charge." Therefore, the magnetic field from the RF coil can provide some confinement of the plasma" [13]. and the ion flux to the discharge chamber wall decrease. This is explained by the walls are floating that reduces the current of bipolar electrons entering the discharge chamber wall and thus reduces energy loss. The size of coil and the amount of power affect the magnetic field generated by the RF coil. This is proved through the formula:

$$B[G] = 10^4 \mu_0 N I \quad (3.27)$$

Where I is the coil current, μ_0 is the permeability of free space $\mu_0 = 4\pi \times 10^{-7}$ H/m and N is the number of turns per meter. The ion and electron velocities in the radial direction are calculated in order to the ion loss across the magnetic field to the wall [22]. The steady-state transverse electron equation of motion includes electron neutral and electron collisions follow this equation:

$$mn \left(\frac{dv_e}{dt} + (v_e \otimes \nabla) v_e \right) = -en(E + v_e \times B) - kT \nabla n \quad (3.28)$$

$$-mnv_{en}(v_e - v_0) - mn(v_e - v_i) = 0$$

$$v_x + \mu_e E + \frac{e}{mv_e} v_y B + \frac{kT}{mv_e} \frac{\nabla n}{n} - \frac{v_{ei}}{v_e} v_i = 0 \quad (3.29)$$

$$v_y + \mu_e E - \frac{e}{mv_e} v_x B + \frac{kT}{mv_e} \frac{\nabla n}{n} - \frac{v_{ei}}{v_e} v_i = 0 \quad (3.30)$$

Where $v_e = v_{en} + v_{ei}$ and $\mu_e = e/mv_e$ and $v_0 \ll v_e$. The transverse electron velocity we have:

$$v_e(1 + \mu_e^2 B^2) = \mu_e \left(E + \frac{kT}{e} \frac{\nabla n}{n} \right) + \frac{v_{ei}}{v_e} v_i \quad (3.31)$$

We equate the electron and ion transverse velocities when assuming ambipolar diffusion:

$$v_i = \frac{\mu_e}{\left(1 + \mu_e^2 B^2 - \frac{v_{ei}}{v_e}\right)} \left(E + \frac{kT}{e} \frac{\nabla n}{n} \right) \quad (3.32)$$

The radial diffusion length in the magnetic field is $l = \nabla n / n$, which is also the last term with the density gradient term. The dipole flow is maintained by an established radial E-field, which also determines the transverse electron mobility. To reduce the maintenance of the dipole, the electric field strength is placed in the region oriented by the horizontal magnetic field and the dipole current in order to reduce the acceleration of the ions towards the wall. "However, in the

limit of no magnetic field, the electric field must accelerate the ions only to the Bohm velocity “[23]. So, the net electric field in the plasma edge region will be limited to:

$$E = -\frac{1}{el} Mv_i^2 \quad (3.33)$$

The minimum magnetic field given by:

$$B = \frac{v_e m}{el} \sqrt{\frac{e}{mv_e v_i} \left(\frac{T_e}{1} - \frac{mv_i^2}{el} \right) - \left(\frac{v}{1+v} \right)} \quad (3.34)$$

The transverse ion velocity to the wall is:

$$v_i = \frac{1}{2} \sqrt{\left[\frac{el}{M\mu_e} \left(1 + \mu_e^2 B^2 - \frac{v_{ei}}{v_e} \right) \right]^2 + \frac{4kT_e}{M} - \left[\frac{el}{2M\mu_e} \left(1 + \mu_e^2 B^2 - \frac{v_{ei}}{v_e} \right) \right]} \quad (3.35)$$

The parameters in the term $v_e = v_{en} + v_{ei}$ and $v = v_{en}/v_{ei}$ are given by:

$$v_{en} = \sigma \sqrt{\frac{8eT_e}{\pi m}} \quad (3.36)$$

$$\sigma = 6.6 \times 10^{-19} \left(\frac{T_e}{4} - 0.1 / \left(1 + \frac{T_e}{4} \right)^{1.6} \right) \quad (3.37)$$

$$v_{ei} = 2.9 \times 10^{-12} \frac{n_e \ln \Lambda}{T_e^{1.5}} \quad (3.38)$$

$$\ln \Lambda = 23 - 0.5 \ln \left(\frac{10^{-6} n_e}{T_e^3} \right) \quad (3.39)$$

In which $\ln \Lambda$ is the Coulomb logarithm. A confinement factor f_c was created to evaluate the decrease in ionic flow to the wall. The simple problem is to compute the expected decrease in the flow of ions to the wall due to a decrease in radial Bohm velocity at a certain magnetic field strength B . In this case, the ions will lose the wall. In this case, the ions that have been trapped into the discharge chamber wall will eventually reach the grids because the axial pre-radial potential generated by the ionic flow towards the grids promotes the axial ion velocity in the plasma. exceeds the radial ion velocity.

3.4 Model and result

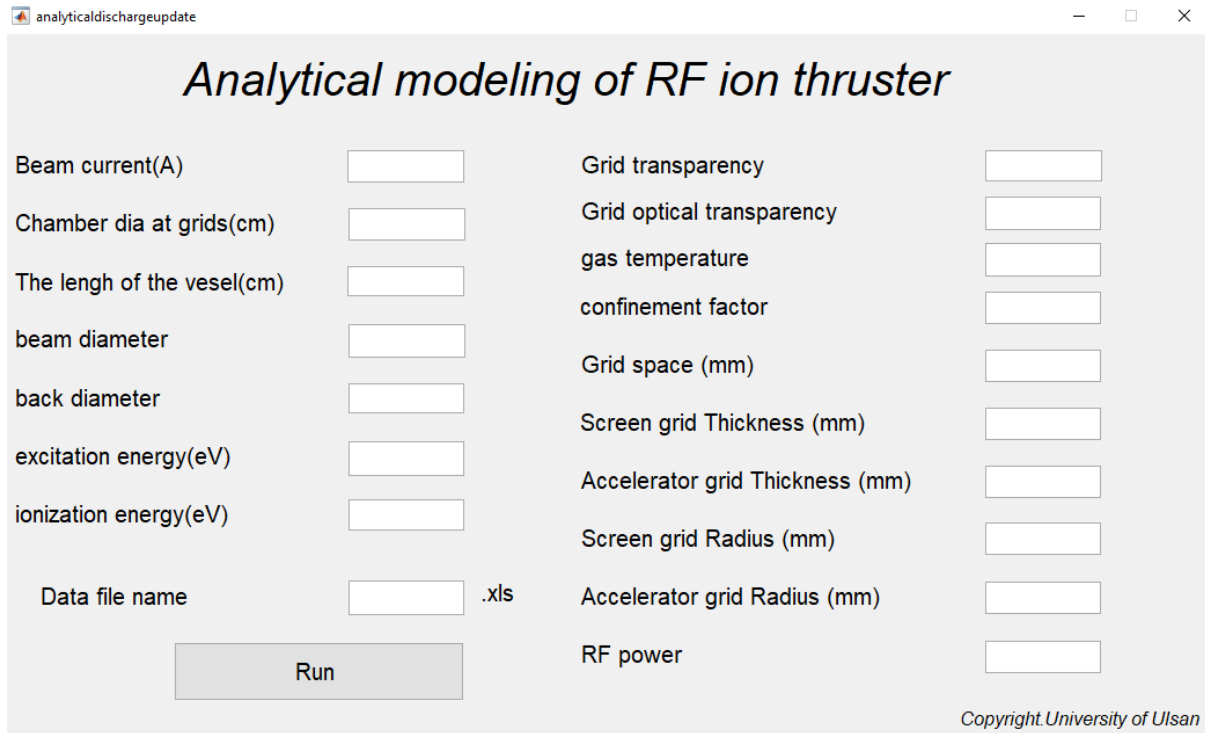


Fig. 3.3 *The interface of Theoretical Analysis Tool Development*

The performance of the RF ion thruster is basically divided according to the characteristics of the RF vibration isolation. Therefore, for the performance analysis of the RF ion thruster, we are developing a theoretical analysis tool based on the analysis of RF discharge. In the previous year, the usable level of code development was completed, and in this year, the theoretical benefit tool was developed based on GUI to make it more intuitive and convenient to use. Fig3.3 is the developed theoretical interpretation. This is a picture showing the GUI panel of the tool. If the line parameters are selected and executed, the calculation result is hindered by the data file in Excel format. Ice oil is set as the main input value, excluding the number of years of the model, and calculation results according to various propellant efficiencies are provided for cases that benefit from each beam advance.

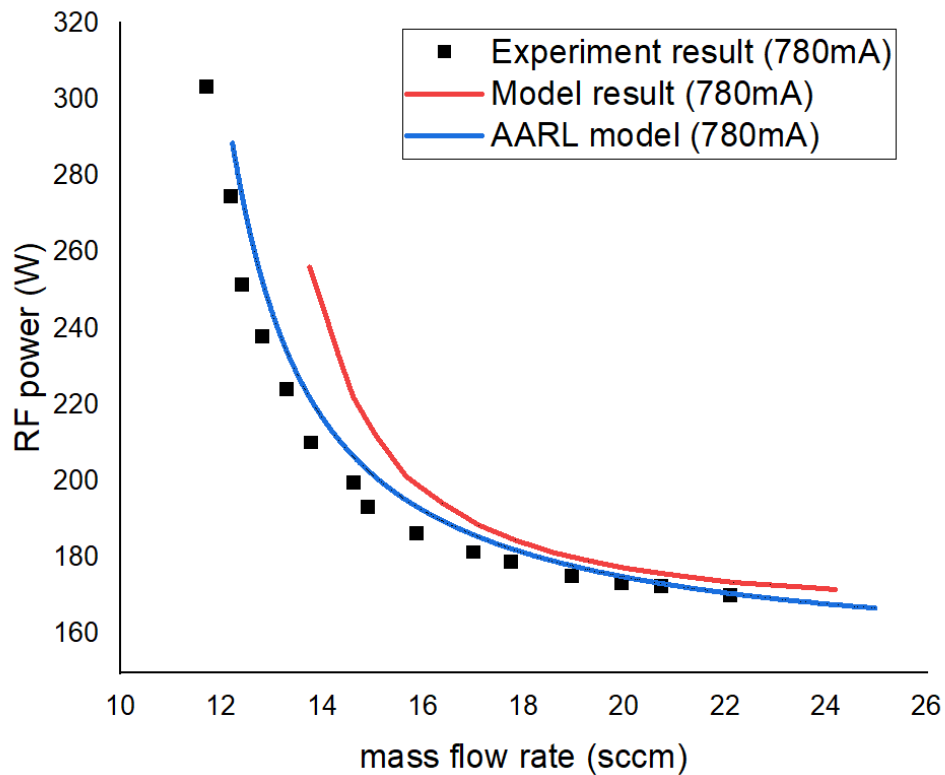


Fig. 3.4 Comparing the calculations obtained from the models with the experimental results of ESA-XX at 780 A

The discharge power curves for the RF thruster ESA XX (current 780mA) are shown in figure 3.4. The square dot curve corresponds to the experimental results [24], the solid red curve corresponds to the mathematical analysis model calculation from Reference. [21] and a solid blue curve that corresponds to our model calculation. Figure 3.4 also shows that we provide a better result even in the case of a lower flow rate.

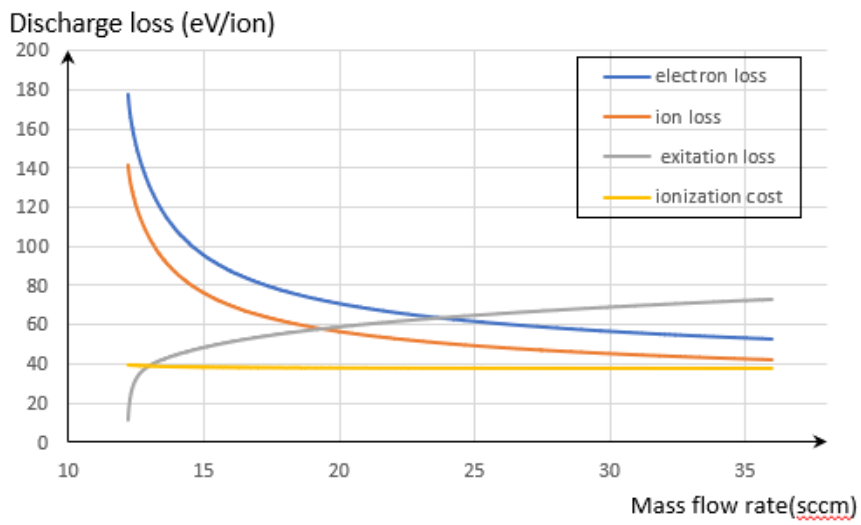


Fig. 3.5 The ion production cost channels map of the ESA-XX RF ion thruster at $I_b=0.78 A$ obtained by our analytical model.

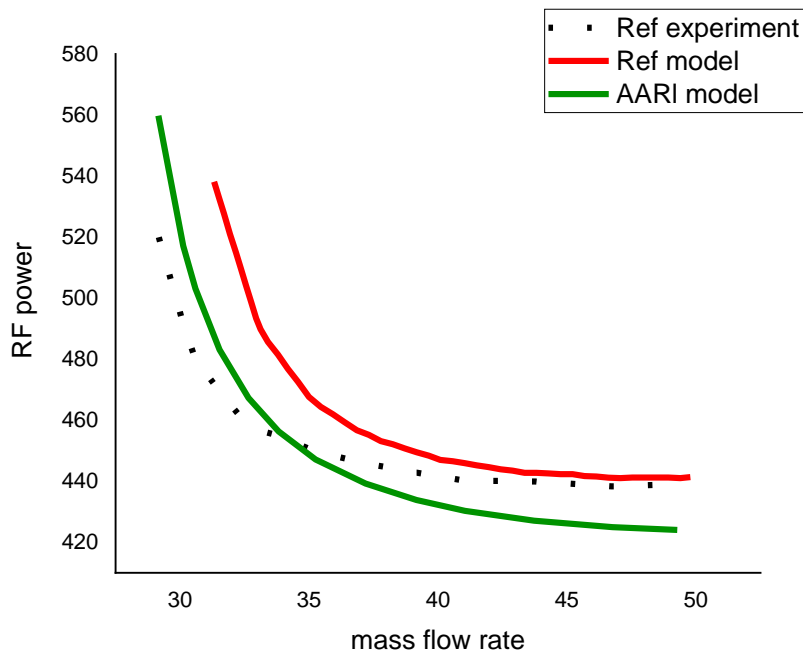


Fig. 3.6 Comparing the calculations obtained from the models with the experimental results of ESA-XX at $I_b = 2\text{ A}$

Fig. 3.6 shows a comparison of the calculations obtained from the models with the experimental results of ESA-XX at $I_b = 2\text{ A}$. In which the error from our calculation model with experimental results is about 0.31% to 7.67% with $I_b = 2\text{ A}$, the size of the ion thruster in the test is 26cm in diameter (ESA-XX).

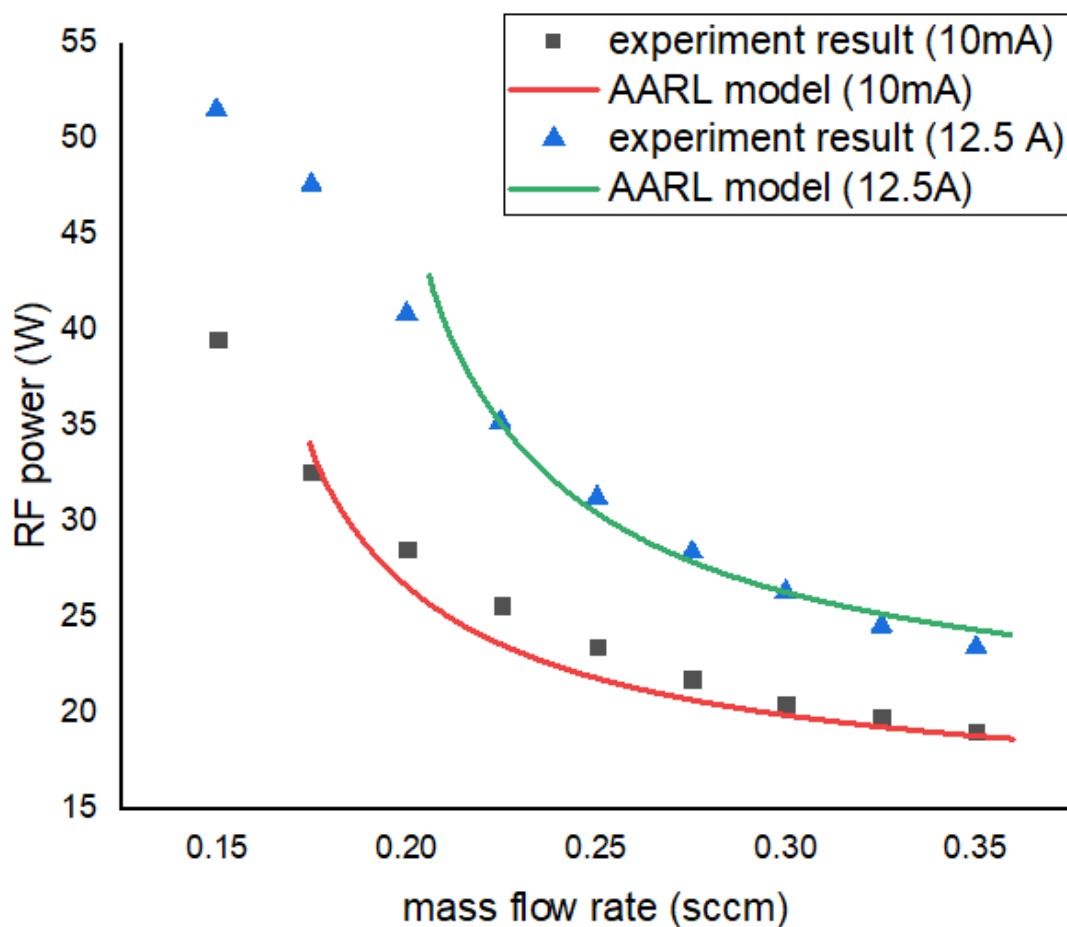


Fig. 3.7 Comparing the calculations obtained from the models with the experimental results of RIM-4 at $I_b = 10\text{mA}$ and $12,5\text{mA}$

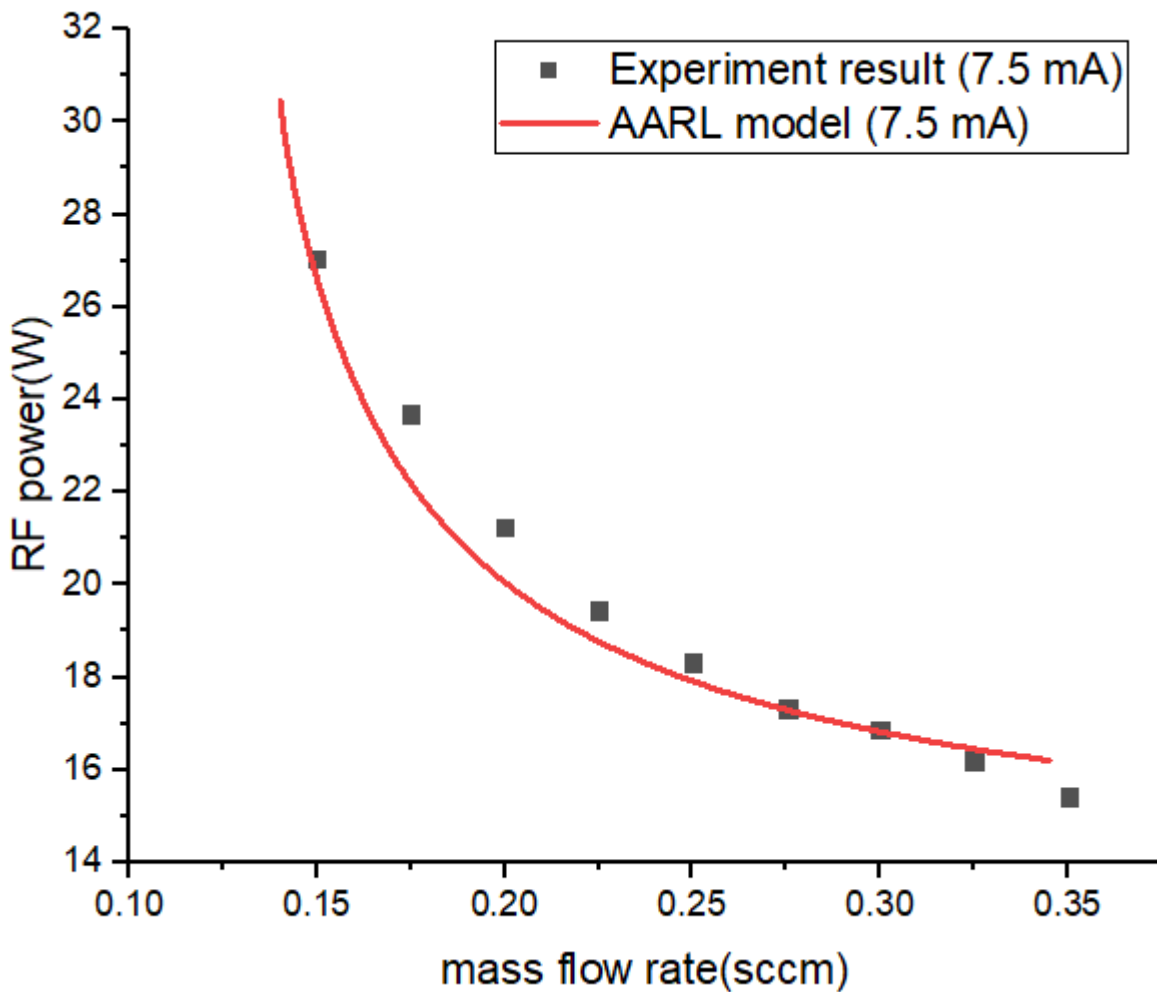


Fig. 3.8 Comparing the calculations obtained from the models with the experimental results of RIM-4 at $I_b = 7.5\text{mA}$

Figures 3.7 and 3.8 show the calculation results on our model and experimental results for the power requirement and low mass flow rate have both errors below 10%. The ion thruster mentioned in this experiment is the 4 cm diameter RIM-4 with a spherical discharge chamber. Based on the above comparison results, our analytical model is in good agreement with the experiment and not depend on scale.

Our model helps to optimize the design process such as choosing motor geometry. Figure 3.9 shows efficiency for various area ratio when the same RF power and other values like screen diameter, beam current, etc.

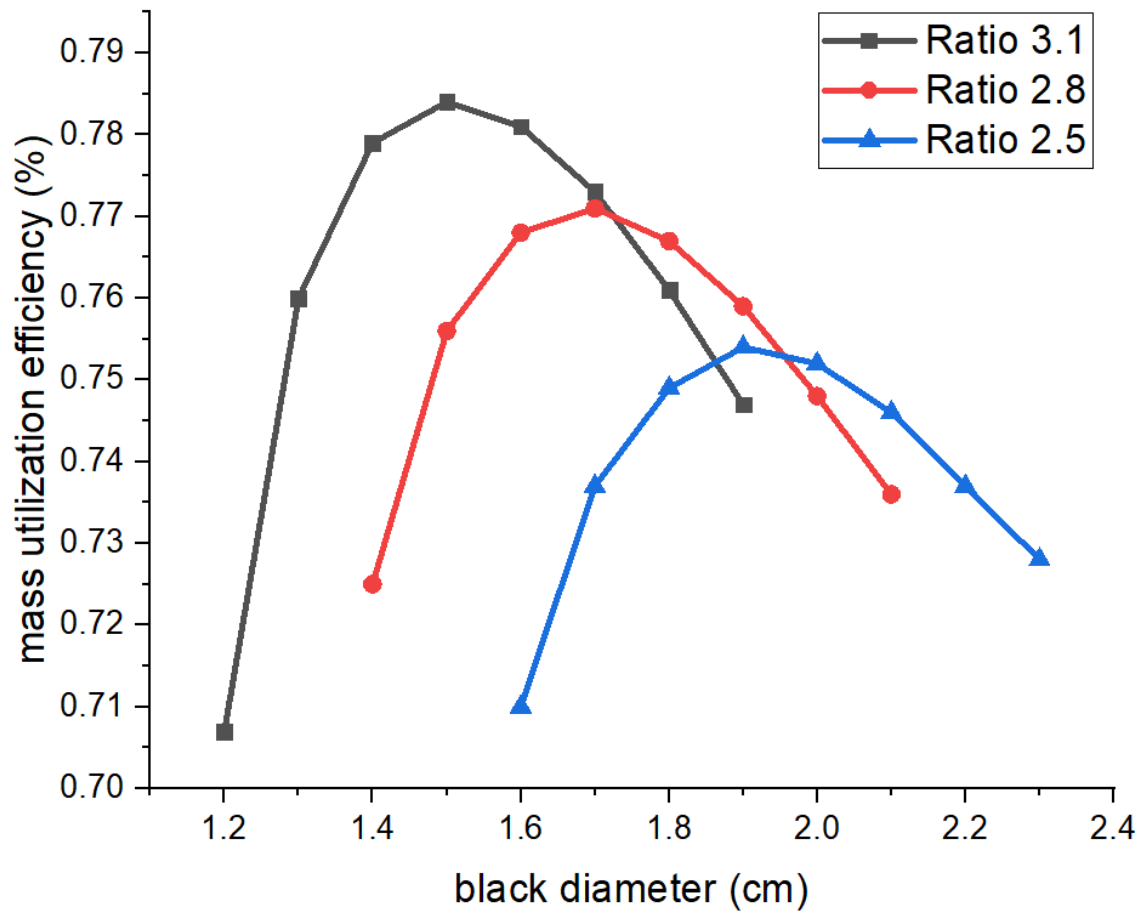


Fig. 3.9 Efficiency for various area ratio.

3.5 Summary

An analytical model for the ion thruster is built to provide a better predictor of performance during the design process. The additional feature that we have considered in this model is the transformational coefficient obtained from the Monte Carlo calculation. The model created on MATLAB Guide app makes it is easy to use, and it's also, compared to previous analytical

models, it is commonly used in laboratories. The calculation results obtained from our analytical model obtained good results consistent with the experimental results for RF thrusters for different beam currents and sizes of thruster.

Chapter 4. Measurement system

4.1 Faraday probe

4.1.1 Formation of Faraday probe

The Faraday probe system is used to measure ion beam current. The structure of the Faraday probe includes a collector enclosed in a guard ring between them there is an insulator. [25-27] When ion beam goes through grids of RF thruster to Faraday probe. It is absorbed into the collector, besides low energy ions coming from non-axial directions are absorbed by a guard ring. The current density is evaluated by measuring the ion current received and divided by the collector surface area. Measurements are made by varying the distance between the engine and the Faraday probe and varying the flow rate and RF power. The ion beam current can determine the divergence angle of the ion beam of the RF thruster.

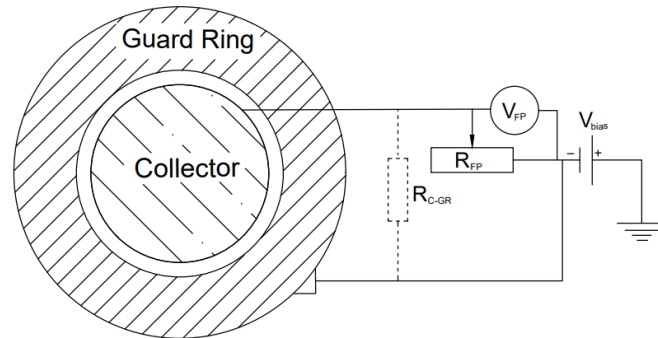


Fig. 4.1 The schematic of the Faraday probe

Ion current density is calculated to follow equation:

$$j = \sum_k e \Gamma_k Z_k = \frac{I_{EP}}{A_C + k_G} k_{SEE} \quad (4.1)$$

I_{EF} is ion current of a point measurement by the Faraday probe at (Z,r) , k_G is correction for probe ion collection area, k_{SEE} is correction for collector secondary electron emission.

$$k_G = \pi (R_{GR}^2 - R_C^2) \left(\frac{2\pi R_C h_C}{2\pi R_C h_C + 2\pi R_{GR} h_{GR}} \right) \quad (4.2)$$

$$k_{SEE} = \frac{1}{1 + \Sigma_k \frac{\Omega_k \gamma_k}{z_k}} \quad (4.3)$$

R_C is radius of collector, h_C height of collector, R_{GR} is radius of guard ring and h_{GR} is height of guard ring.

Total ion beam current near field:

$$I_b = 2\pi \int_0^{\infty} J[r] r dr \quad (4.4)$$

Total ion beam current far field:

$$I_b = 2\pi R^2 \int_0^{\pi/2} J[\theta] \frac{k_D}{k_A} \sin(\theta) d\theta \quad (4.5)$$

4.1.2 Design Faraday probe for RF thruster.

Faraday probe can negatively affect the plume measurements if plasma disturbances are caused. A probe design must satisfy the following conditions: receiver diameter, distance between receiver and guard ring, probe material, voltage deviation. Ions have low energy from non-axial directions by a guard ring cover the collect contemporaneous which reduce electrostatic edge effects. Part of ions when to Faraday probe go to gap between collector and guard ring so minimized to overlap which have value approximately 5 to 10 with the local plasma Debye length.

Equation for calculating Debye length is presented:

$$\lambda_D = \sqrt{\frac{\epsilon_0 k T_e}{n_e e^2}} \quad (4.6)$$

T_e is electron temperature, n_e is electron density, Boltzmann constant is k and ϵ_0 is permittivity of free space. Dc power supply provide for collector and guard ring is -15V to -30V far field measurements and approximately 100V for near field measurements. The value of resistor (R_{FP}) is from 10 Ω to 1000 Ω .

Table 4.1 *Manufacturing paraments of Faraday probe*

COMPONENT	VALUE
Diameter collector	1 cm
Diameter guard ring	2 cm
Distance between collector and collector	1mm

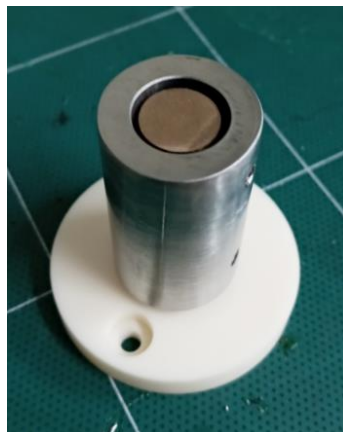


Fig. 4.2 *Faraday probe of ARRL lab*

The parameter prices are based on the reference [27] and the machinability of the factory.

4.1.3 Travel system

In order to measure the ionic density at different positions and the ion distribution we need a travel system. There are two measurement positions of the faraday: near field and far field.

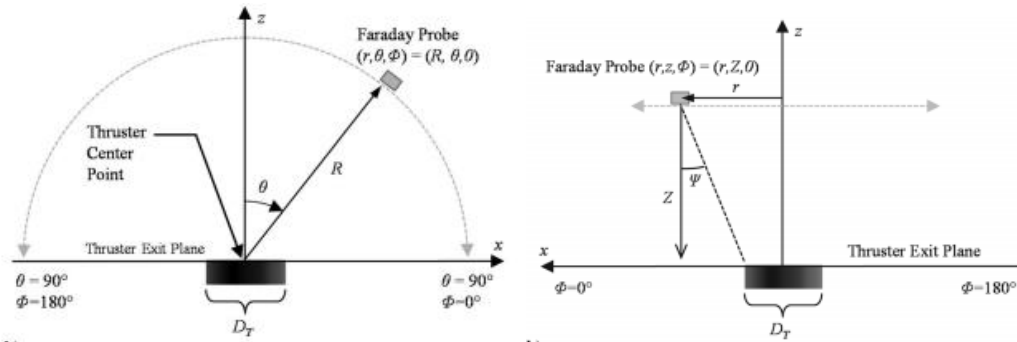


Fig. 4.3 the location of the praday probe[24]

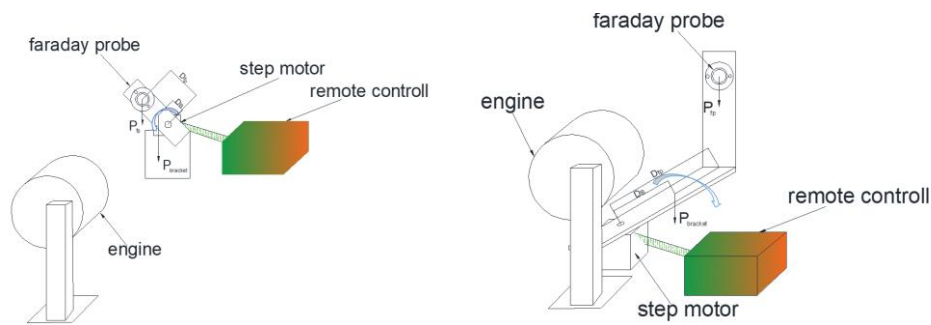


Fig. 4.4 Travel system for Faraday probe : near field (left), far field (right)

Travel system includes Faraday probe holder, remote control, stepper motor. Remote control of step motor includes L298 and Arduino and power supply 6V-12 V. (It is show figure 4.5). Step motor will control by Arduino application or MATLAB by cable USB through Arduino UNO. Step motor was chosen to depend to stall torque which must bigger than moment of gravitation of faraday probe and bracket:

$$P_{fb} \times D_{fb} + P_B \times D_B < T_{sm} \quad (4.7)$$

- P_{bracket} is gravitation of bracket
- D_{fb} is distance between faraday probe and center of step motor
- D_B is distance between center bracket and step motor.
- P_{fb} is gravitation of faraday probe.

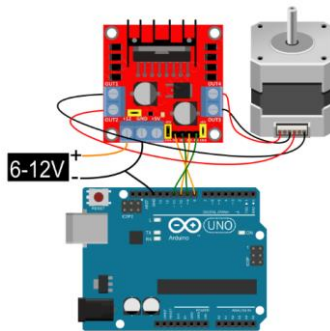


Fig. 4.5 remote control of step motor

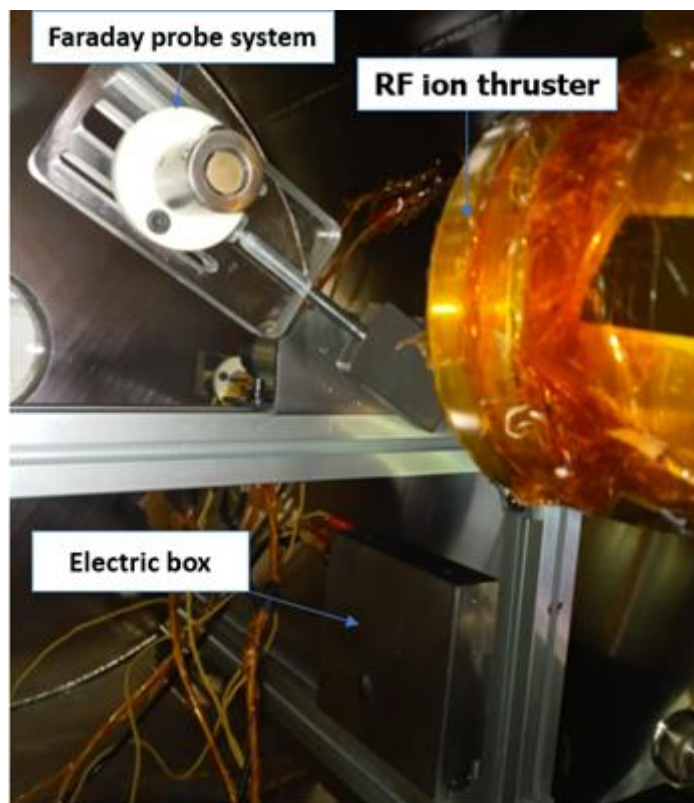


Fig. 4.6 *Travel system in chamber*

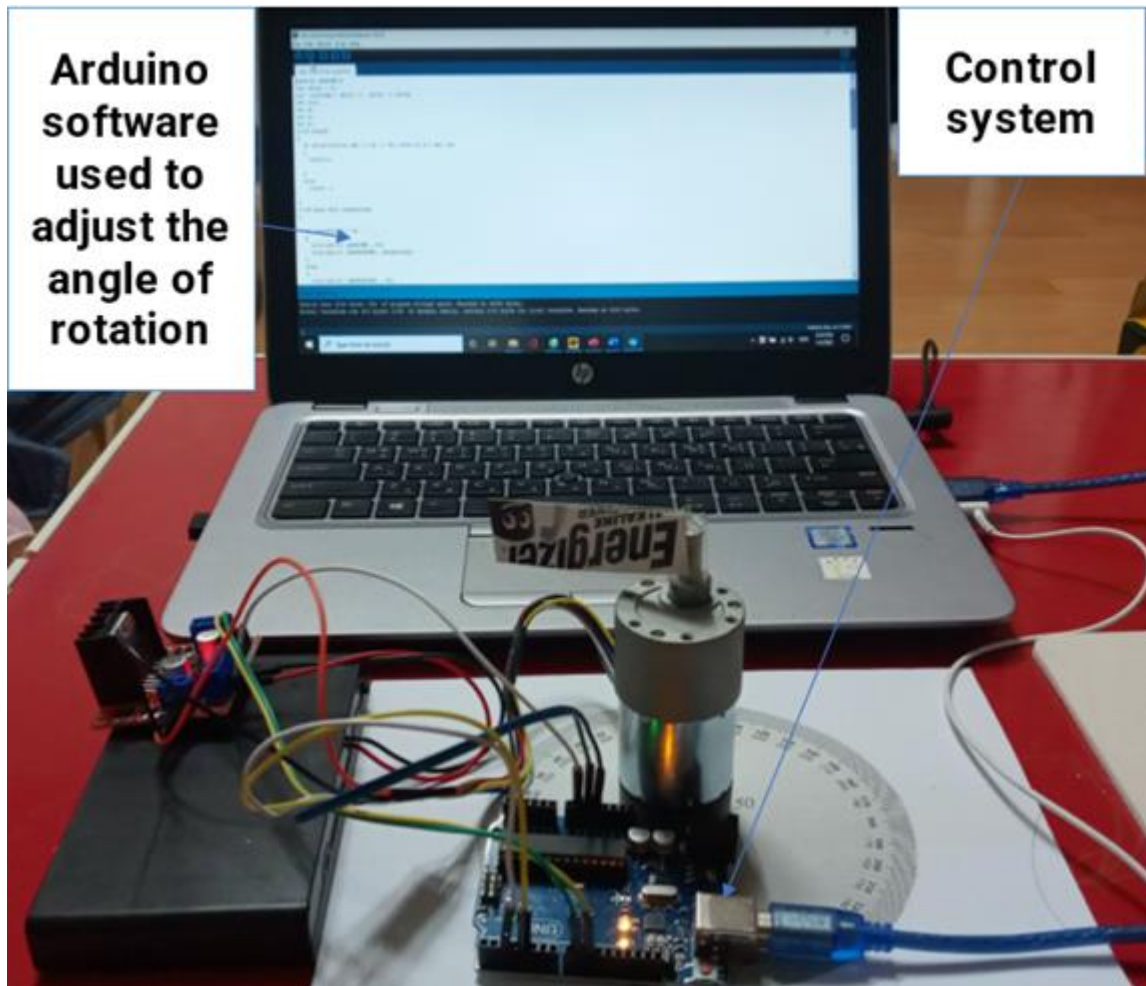


Fig. 4.7 *Control circuit*

The travel system is connected to the control computer outside the vacuum chamber by USB feedthrough.

4.2 RPA probe

4.2.1 *Formation of RPA probe*

The RPA probe system is measuring the ion energy distribution. The structure of RPA probe includes 3 grids, a collector enclosed in a guard ring between them there is an insulator. The first grid is a floating grid used for reducing the plasma perturbation and attenuate the density

in the RPA. The second one, electron repelling grid is negatively biased for repelling the electrons. The third grid has a role to do the ion retarding grid which is positively biased at various high values by sweeping the voltage. At different retarding potentials, the collector will obtain a different current signal. The ion current obtained by the collector is related to the ion velocity distribution given by:

$$I(V) = A_C q_i n_i \int_{u(V)}^{\infty} u_i f(u_i) du_i \quad (4.8)$$

Where A_C is the probe collection area, q_i is the charge-state of the ion, n_i is the ion density, V is the ion retarding, u_i is the ion velocity [28]:

$$u_i = \sqrt{\frac{2q_i V}{M}} \quad (4.9)$$

$$du = \sqrt{\frac{q_i}{2M}} \frac{1}{\sqrt{V}} dV \quad (4.10)$$

$$f(u) du = f(V) dV \quad (4.11)$$

Where $f(V)$ is the energy distribution function. From 4.9 to 4.11,

$$I(V) = A_C q_i n_i \sqrt{\frac{2q_i}{M}} \int_{V_{min}}^{\infty} \sqrt{V} f(V) dV \quad (4.12)$$

Ion energy distribution can be obtained:

$$-\frac{dI}{dV} = \frac{A_C q_i^2 n_i e^2}{M} f(V) \quad (4.13)$$

Where e is the elementary charge and M is the ion mass. Voltage $V = \epsilon_i / e$, ion energy distribution function can be deduced from the function $f(V) = f(\epsilon_i / e)$.

4.2.2 Design RPA probe:

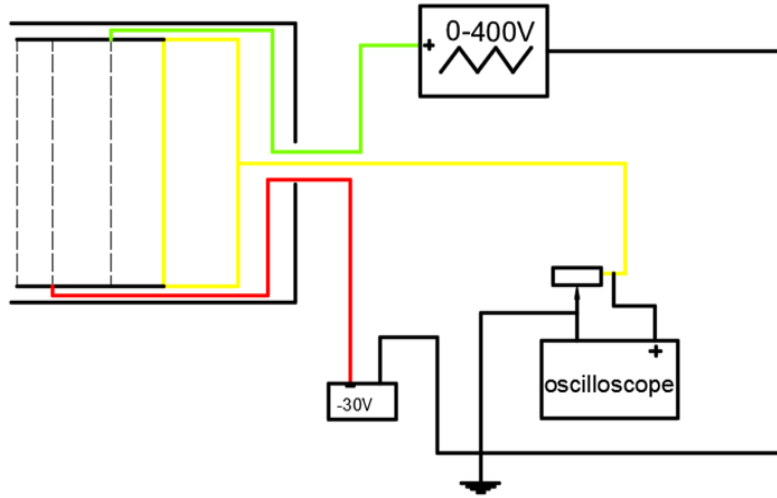


Fig. 4.8 Example for electric circuit of RPA probe

Each grid plays a different role in contributing to the accuracy of the measurement. Along with that, the distance between the grid is also very important because if the distance is too large, it will cause the accumulation of electricity and lose the effect of the grid. Ideally this distance is determined by the following formula:

$$x \approx 1,02\lambda_d \left(\frac{eV_d}{k_B T_e} \right)^{3/4} \quad (4.14)$$

The two factors that determine the size of the mesh in RPA probe is the length of the Debye and the effect of the mesh size of the large mesh and the small mesh. If the mesh hole is too large, ions will pass through the grid due to a decrease of potential at the center of each cell. However, if this size is too small, the increased surface area leads to a decrease in the number of passing particles. To determine the maximum potential deviation around the grid we have the equation:[29]

$$\frac{\Delta V_r}{V_r} = 1 - \frac{2\pi(x|a) - \ln 4}{2\pi(x/a) - 2 \ln(2 \sin(\pi r/a))} \quad (4.15)$$

As the mesh becomes larger there will be a greater number of particles that can pass through due to reduced physical obstacles, creating a larger measurable current on the meter. more particles will pass through. This causes inaccuracies to the measured currents.

Table 4.2 *Manufacturing parameters of RPA probe*

<i>PARAMETER</i>	<i>VALUE</i>
Diameter collector	1 cm
Diameter hole of grid	0,05 cm
Distance between floating grid and repelling grid	1 cm
Distance between floating grid and regarding grid	2cm
Distance between floating grid and collector	3cm
Diameter of guard ring	2.2cm

The parameter prices are based on theory and the machinability of the factory.

4.3 Development of Torsional Thrust Stand

The thrust stand, which makes it possible to measure the thrust by changing the thrust generated by the ion engine into rotational motion, was designed as a torsion type, and while continuously improving the previous model, the neck design was changed so that it can be installed inside the vacuum chamber. Fig. 4.9 is a diagram showing the shape of the thrust strand of torsion time designed according to the size of the vacuum chamber possessed. To improve the measurement level of the force generated by the thruster, the length from the pivot spring could be asymmetrical, and a gong electric pin could be installed at one end and a thruster could be installed at the other end. In order to reduce the rotational vibration caused

by the pivot spring, a magnetic field damper was installed, and the displacement of the thrust stand was measured in real time with a laser displacement meter.

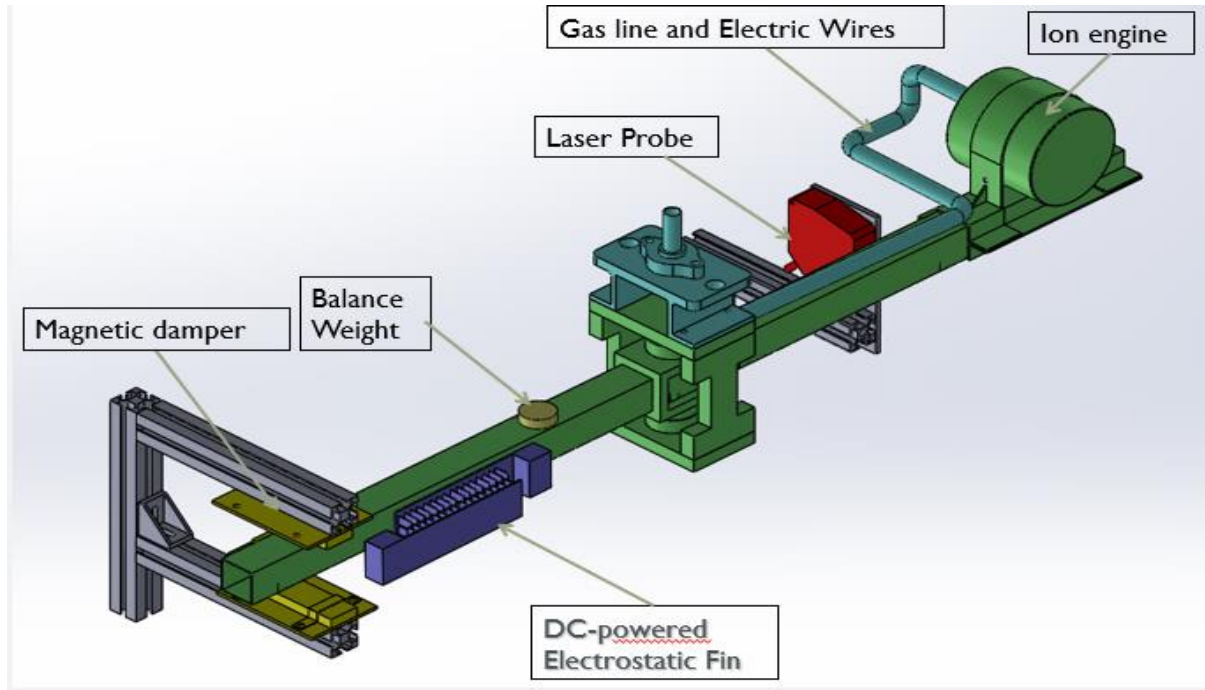


Fig. 4.9 Shape drawing of the thrust stand installed inside the vacuum chamber

4.3.1 Torsion balance dynamics

The Thrust stand consists of a hollow square bar of length $L = 1000$ mm and torsion spring providing the restoring torque. When the engine works, a thrust causes the swing arm to tilt at an angle. This inclination will be measured with a distance-measuring laser sensor. We have the natural frequency of the system:

$$\omega_n = \sqrt{\frac{k_\theta}{I_\theta}} \quad (4.16)$$

Where k_θ is the torsion spring constant and I_θ the moment of inertia (MI) of the system. However, in order for the system to stabilize we need damping, facilitating quick readings. Then, the motion equation is:

$$\ddot{\theta} + 2\zeta\omega_n\dot{\theta} + \omega_n^2\theta = \frac{f(t)l_T}{I_\theta} \quad (4.17)$$

Where $\theta(t)$ is the instantaneous deflection angle, $f(t)$ is the time dependent force, ζ is the damping coefficient and l_T is (moment arm) the distance from the pivot at which the force forms a torque. The steady state solution given by [30] (using small angular displacement $\theta = \frac{x}{l_T} \frac{180}{\pi}$):

$$\theta(t \rightarrow \infty) = \frac{Fl_T}{k_\theta} \Rightarrow F = \frac{\theta(\infty)k_\theta}{l_T} \Rightarrow F = \frac{k_\theta x}{l_T l_s} \frac{180}{\pi} \quad (4.18)$$

Based on the formula 4.18, we can see when knowing the linear displacement in steady state can easily calculate the force F. Maximize the resolution of force can be done by two ways: using torsion springs with constant Low spring count or increase Momen length and sensor distance. Due to the volume limitation inside the vacuum chamber will limit the torque length and inner sensor distance. The spring selected has a rated spring constant of 5.4232 N-mm / Degree ensuring a load capacity of 15 kg.

4.3.2 PCB electronic comb

In the process of studying the development of the RF ion engine [31], we face a great challenge when measuring their repulsive force. The force generated by these motors is about micro-Newton, requiring a simple, low-cost force measurement method to solve this problem. An electrostatic calibration technique is highly flexible in producing a wide different range of force and they have widely applied measurement from nano-Newton to micro-Newton thrust stand calibration. Based on the printed circuit board and commercial fins, the comb can be realized flexibly with the conveniently extended output force. Differences from the traditioned conductive area of the comb fixed plate are minimized to improve the force consistency over engagement.

In the paper, we focus on simulation about PCB electronic comb [32] and introduce the magnetic structure of the measuring system.

The expression must be generalized to a line integral:

$$V_f - V_i = \int \vec{E} \cdot d\vec{s} \quad (4.19)$$

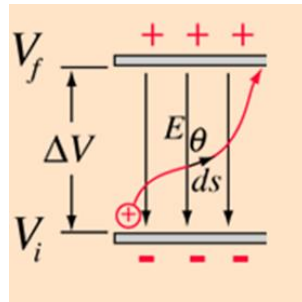


Fig. 4.10 Relationship between electric field and electric potential

The PCB electrostatic comb calibration system consists of a PCB electrostatic comb, a function generator, a high voltage power supply, a high voltage measurement probe and an oscilloscope. The high voltage pulse generator is presented in figure 4.11.

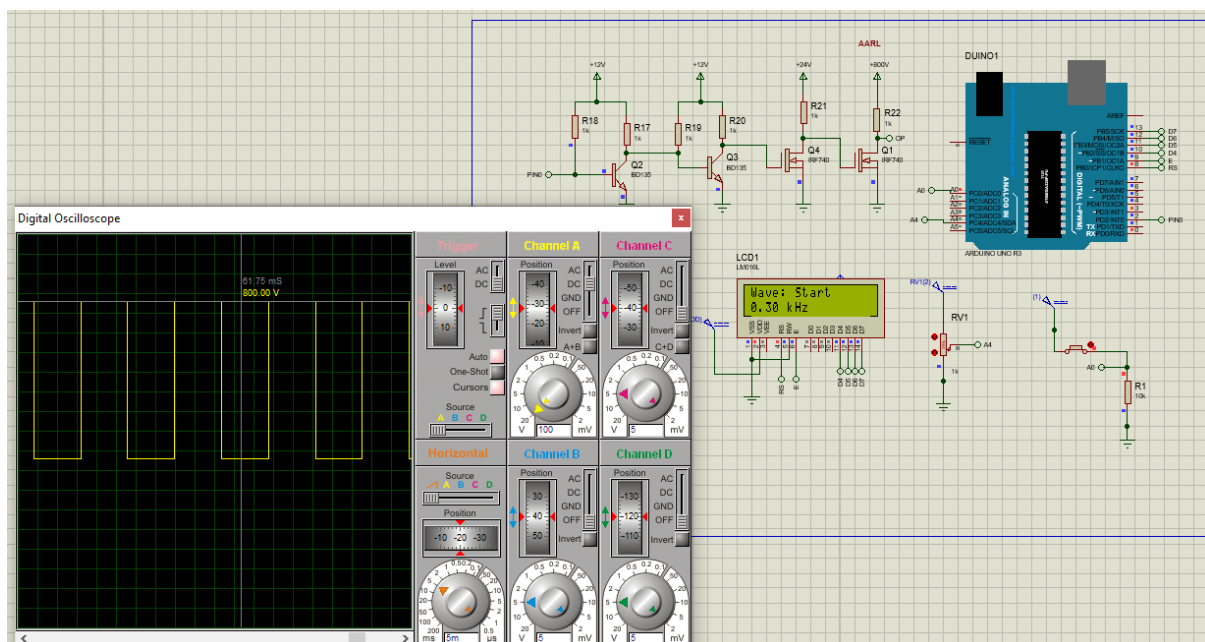


Fig. 4.11 *Simple AARL fin comb circuit*

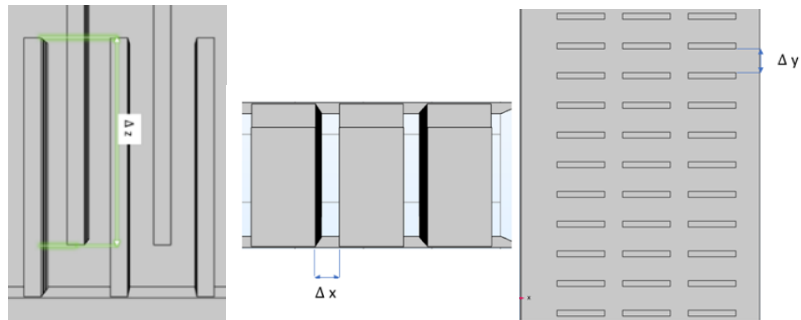


Fig. 4.12 : *Layout of the polar plate*

With the drive signals produced by the function generator, the NMOSFET is triggered. The width of the square pulse can be changed by adjusting the interval of the signal. The amplitude of the output voltage could be adjusted from 0 V to 2000 V, and the pulse width of the square waveform could be from hundreds of nanoseconds to seconds. The comb can generate a steady-state force when supplied with a DC voltage and an impulse output with the high voltage square waveform [33-34]. A damping resistor (500Ω , 5 W) is connected in series between the comb and voltage power source to reduce the voltage overshoot. The voltage probe is used to measure the output voltage of the power source and the pulse width of the square waveform in high voltage. To ensure the accuracy of the measurement, the probe and the oscilloscope is calibrated beforehand.

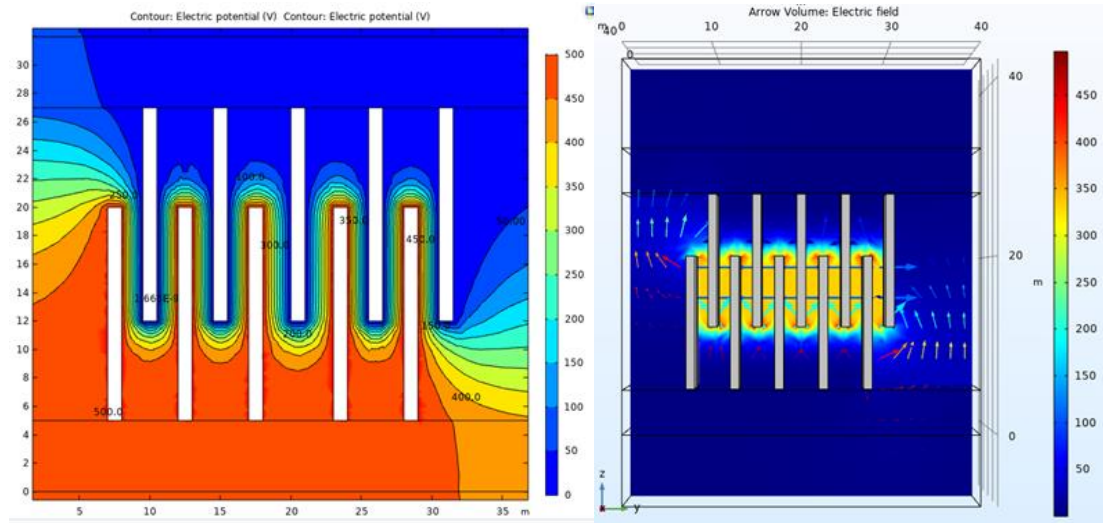


Fig. 4.13 *Electric potential and electric field*

Figure 4.13 shows the electric potential and electric field of PCB electronic comb. The parameter of PCB electronic comb is the distance between poles, following axis x, y, z which are $\Delta x = 2$, $\Delta y = 5$, $\Delta z = 8$. One pole is grounded, and another pole is connected to the source with $V = 500V$ (waveform square)

In the simulation model for the experiment, the fins are designated as aluminum, and the surrounding medium is air, as depicted in Figure 4. The charged fin is assigned an excitation voltage from 0 – 1000 V with a square pulse. The frequency is set to be 500KHz. The same procedure is used for the simulation in COMSOL software, COMSOL Inc.

We consider each pair of poles as two parallel wires where the electromagnetic forces should appear. The polar plates are shaped as shown in Figure 4.14.

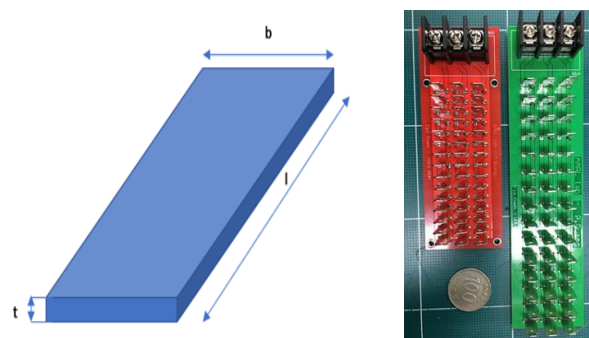


Fig. 4.14 Shape the polar plates

We have self-inductance of the polar plate [35]:

$$L = \mu_0 \cdot 2 \cdot l (\ln 2l / (b+t) + 0.5) \quad (4.20)$$

This energy is stored in the magnetic field \vec{B} of the inductor [36]:

$$W_m = n \frac{1}{2} LI^2 = \int \frac{1}{2} \mu H^2 dv = \int \frac{1}{2} \frac{B^2}{\mu} dv \quad (4.21)$$

Ampère's Law equation:

$$\oint H dl = \int_S J dS \quad (4.22)$$

Where μ is the permeability of the medium and \vec{J} is the externally applied current.

The volume electromagnetic force density is given by:

$$\vec{F} = \vec{j} \vec{B} \quad (4.23)$$

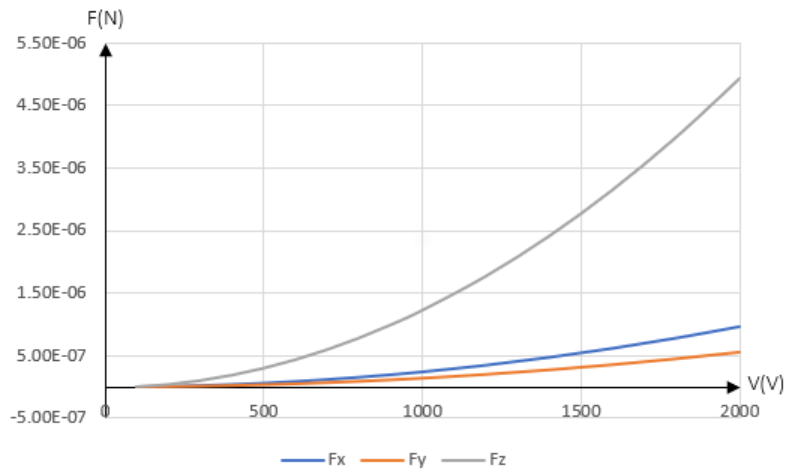


Fig. 4.15 The graph represents the relationship of Δz and electromagnetic force at $V_0 = 1000V$

When Δz changes, the volume changes; we have magnetic field changes according to the equation (4.21).

4.4 Summary

An ion beam current measurement system including a Faraday cup and travel system is designed and completed. Along with that, the system and RPA probe system are designed and manufactured for ion energy distribution measurement. This chapter also presents the development of the Torsional Thrust Stand system for measuring thrust of the engine.

Chapter 5. Simulation and experiment

5.1 Simulation and experimental equipment

The code simulates the ion trajectories through the screen grid and acceleration grid of the RF ion thruster. The simulations utilized the 2-D axisymmetric model, with the axis is the x-axis. Figure 5.1 describes the model of the simulation.

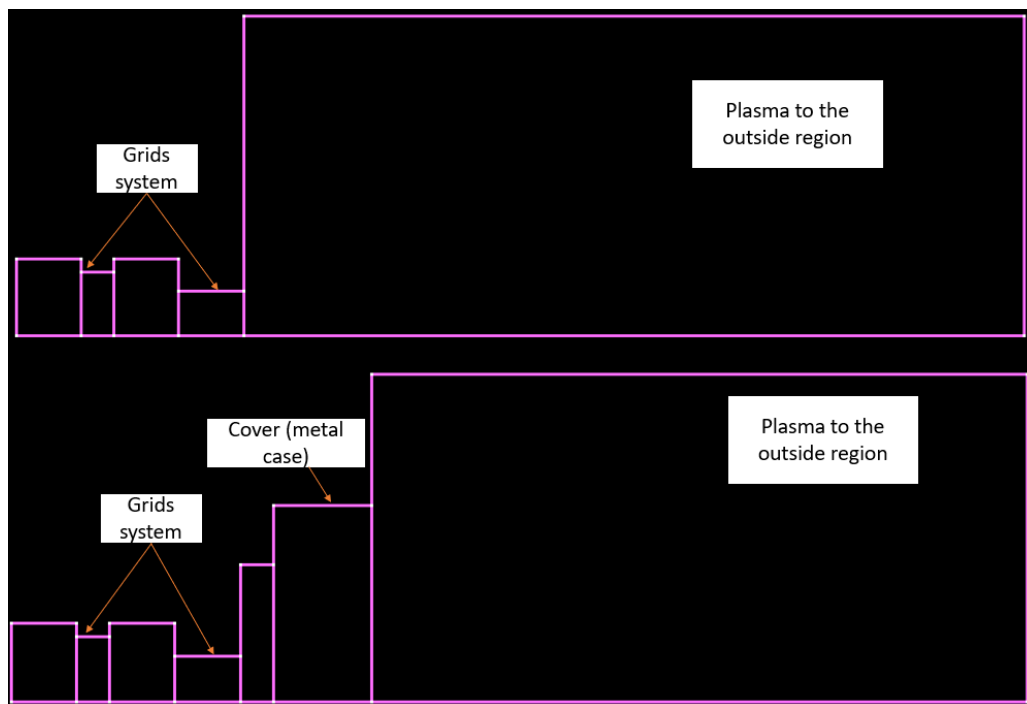


Fig. 5.1 : *Simulation geometry model*

Mesh file generated by the VizMesh2D geometry creation and meshing software. A grid has been created for the computational domain. The smallest edge mesh element has a value of 0.025 (mm). The cell element type is square elements.

Particle In-Cell Model (PIC) was used in this study, in this simulation all charge carriers are modeled as particles and the motion of charge carriers is driven by an electrostatic field [38-40]. Gauss's law of electromagnetism, i.e., Poisson's equation is used to determine the self-consistent electrostatic potential ϕ :

$$\vec{\nabla} \cdot (\epsilon_r \vec{\nabla} \phi) = -\frac{\rho_c}{\epsilon_0} \quad (4. 24)$$

where, ϵ_r is the relative dielectric permittivity of the material, ϵ_0 is the dielectric permittivity of vacuum and ρ_c is the space charge density. The self-consistent electrostatic field $\vec{E} = -\vec{\nabla} \phi$ the particles considered in this study are all Xe+ charged particles, so they are all subject to the Lorentz force:

$$\vec{F}_{Lorentz} = Z_p (\vec{E} + \vec{c} \times \vec{B}) \quad (4. 25)$$

The space charge density in the gas is:

$$\rho_c = e \sum_{k=1}^{K_{gas}} Z_k n_k \quad (4. 26)$$

where, Z_k is the species charge number, K_{gas} is overall species and the number of particles in a mesh:

$$n_k = \frac{\sum_{k,p} 1}{V_{cell}} \quad (4. 27)$$

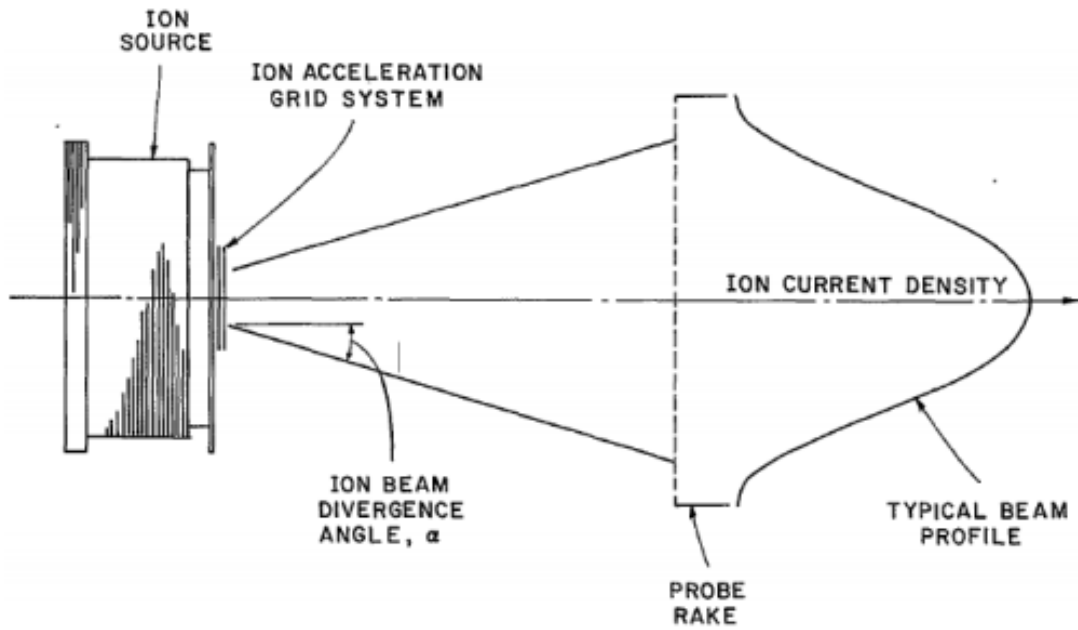


Fig. 5.2 : Method of obtaining ion beam profiles [41]

The angle of divergence is calculated by the formula [41]:

$$\alpha = \tan^{-1}[(R_a - R_B) / L] \quad (4. 28)$$

Where: R_a is radius normal of ion beam current, R_B is ion beam radius at accelerator grid and L is distance from the accelerator grid to the position considering the radius of the ion beam current. Assuming that the plasma densities passing through the acceleration grid are uniform between the holes, in order to determine the angle of divergence we need only consider the outermost hole of the acceleration grid. In this simulation, the outermost hole of the system is taken into research, so the angle of divergence is calculated as follows:

$$\alpha = \tan^{-1}[(R_{ag} - R_{accel}) / L] \quad (4. 29)$$

Where: R_{ag} is radius normal of ion beam current pass through the outermost mesh hole of the acceleration grid, R_{accel} is ion beam radius at accelerator grid hole.

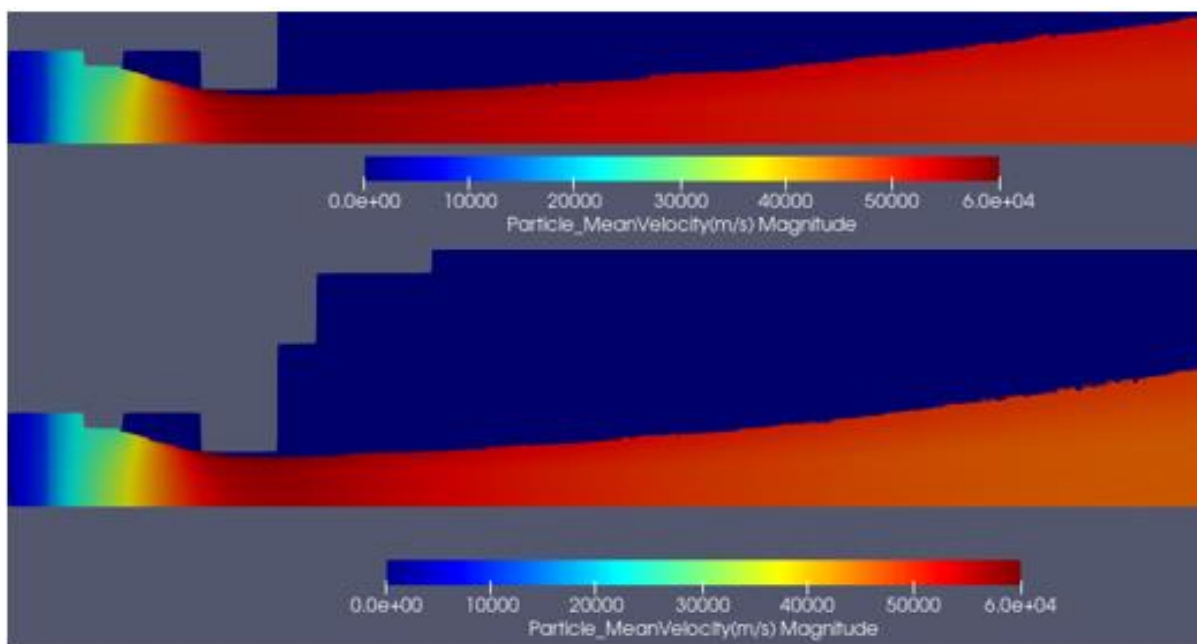


Fig. 5.3 Simulation PIC when there is a shell (lower) and b) in absence of a shell (uper)

The voltage applied to the grid system in the simulation shown in Figure 5.3 is 1500V for positive grid and -350V for negative grid, with source ion is Xenon. In the case of an engine cover, it creates an electrode that attracts ions with the electrostatic force so the divergence angle of the ion beam larger. The divergence of the ion beam to be driven principally by radial electric fields. This is explained because when the RF ion thruster housing connected grounded, it produces an electrode. Figure 5.4 shows that the case without the shell has a lower electric field than the case with the shell, so the electric force acting on the ion is also lower so the divergence angle in case the engine has a cover that is bigger than that of the case without cover.

Based on Fig 5.5, the ratio between the diverging angle of the ion beam when there is the of a shell and absence of a shell increases with reduced negative grid voltage. This is explained because the net-to-total accelerating voltage ratio [41] affects the angle of divergence, the smaller the divergence angle, the greater the impact of the engine cover.

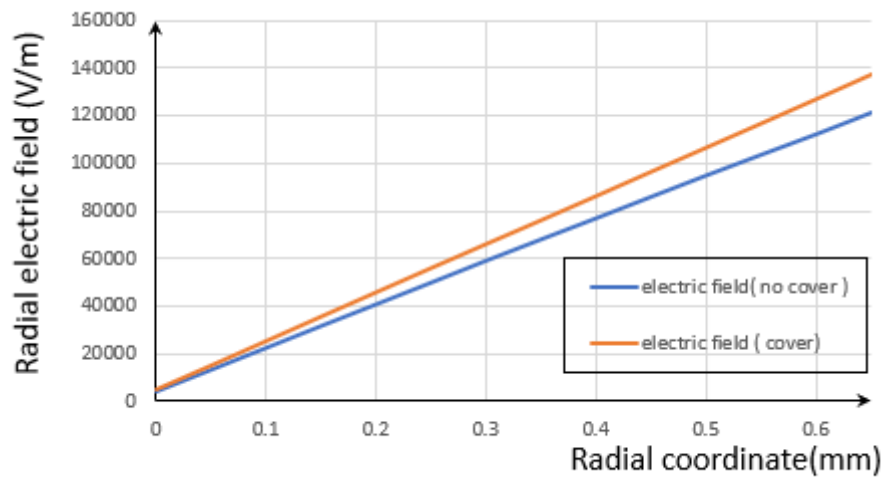


Fig. 5.4 Comparison between electric field (cover) and electric field (no cover) at $z = 2.5\text{mm}$

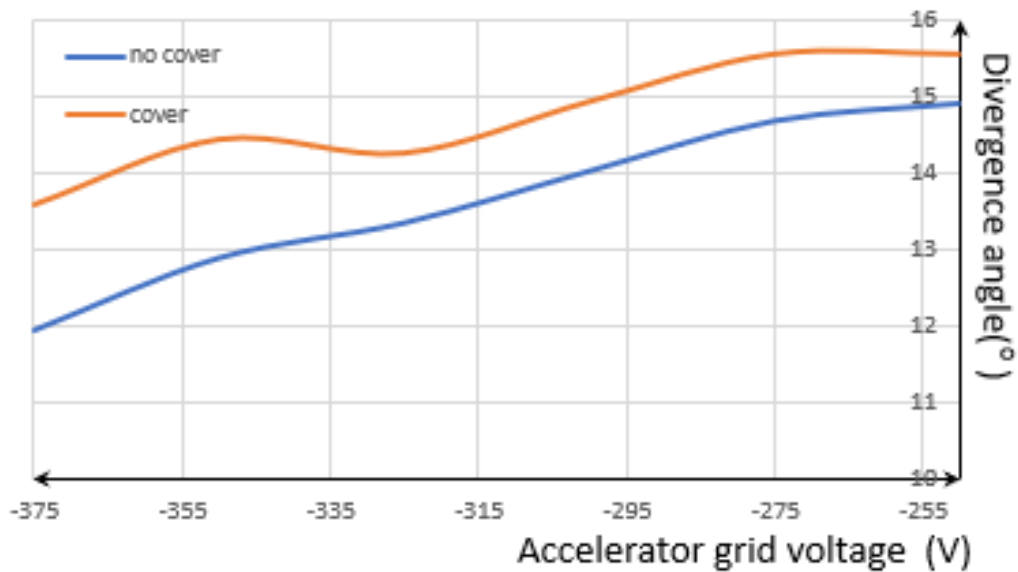


Fig. 5.5 Comparing divergence angle between in case engine have cover and no cover

5.2 Experiment and analysis for Faraday probe.

Faraday probe is kept by feedthrough with insulating jig attached. This insulation is made of alumina ceramic so that it does not produce Eddy currents due to the large magnetic field in the vacuum chamber and high frequency. If Eddy currents appear to cause large noise, it reduces the accuracy of the measurement. Test cases have been done.

Table 5.1 *Parameters in experiment of Faraday probe*

PARAMETER	VALUE
Pressure	6.10^{-6} to 8.10^{-6}(torr)
Probe bias voltage	-100 v
Distance between faraday probe and engine	10 cm
Radial coordinate	0 cm to 7 cm
Mass flow rate	3 sccm to 4 sccm
Rf power	45w to 55 w



Fig. 5.6 : *Experimental images in a vacuum chamber*

Case 1: mass flow rate =4 sccm and change RF power

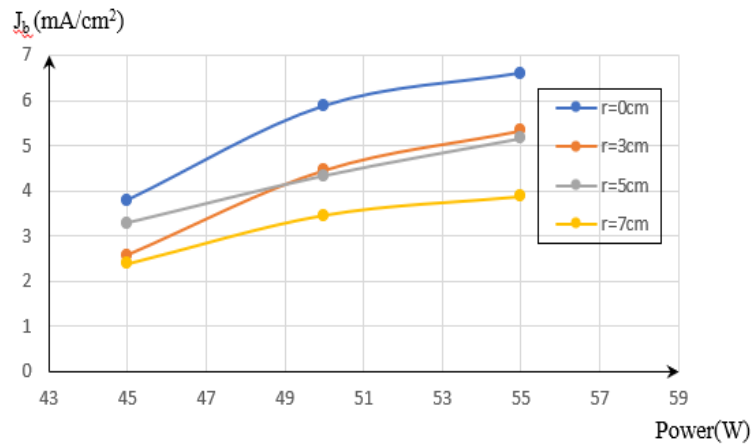


Fig. 5.7 : Result experiment when change RF power

In the case of power changes from 45 W to 55 W with the same mass flow rate of 4 sccm, we get the result that ion current density increases with RF power. The maximal current density (in experiment) is 6.5 mA/cm² at point ($r=0$, flow rate = 4 sccm, RF power = 55W).

Case 2: change flow rate and RF power =50 W.

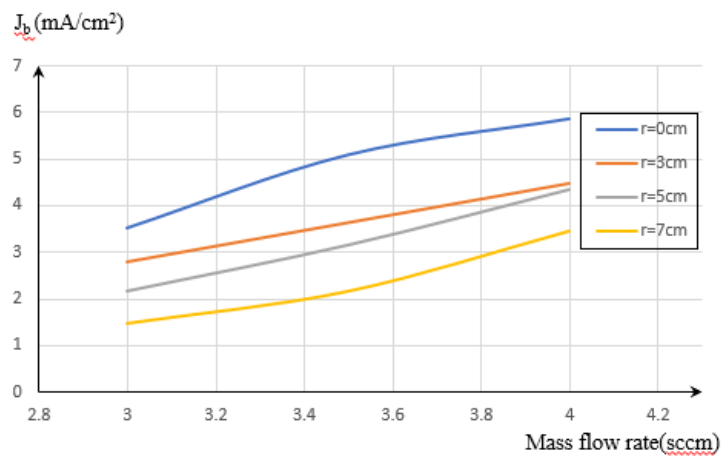


Fig. 5.8 Result experiment when change mass flow rate

The experiment shows that RF power 50W and mass flow rate changed from 3 sccm to 4 sccm; hence, the ion current density gradually increases according to mass flow rate.

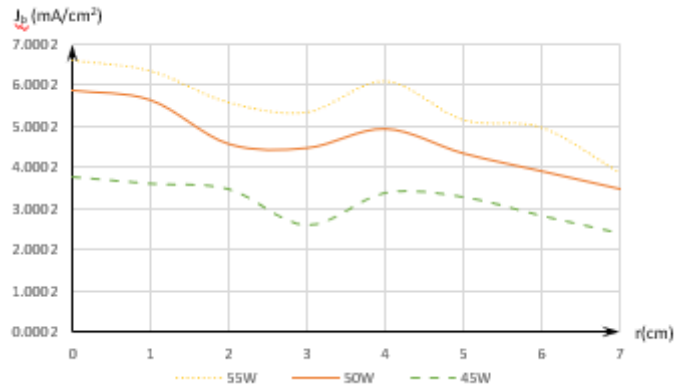


Fig. 5.9 Result experiment when change RF power (set radial coordinate)

Follow Fig 5.9, the ion distribution of the RF ion thrusters generated by AARL differs from the ion distribution tendency of the plasma beam produced in previous studies [42-43]. According to previous studies, the ion density will decrease gradually according to the radial coordinate. However, the engine manufactured at AARL, the ion density reaches a low peak at a position 4 cm from the center of the engine. This is explained by the fact that the RF coil axis deviates from the discharge chamber axis which changes the direction of the magnetic field produced by the RF coil. The Lorentz force [44] is given by:

$$\vec{F}_{LF} = q\vec{E} + q\vec{v}_i \times \vec{B} \quad (5.1)$$

In this case, the force considered is the magnetic force, that impacts only direction of moving charges [45], so the magnitude of the Lorentz force is equal to the charge of the charge of the ion and the vector cross product $v_i \times B$ ($F_{LF} = q \cdot v_i B \cdot \sin\phi$) [44]. The measured deviation angle is about 13.24 degrees, then and the magnetic force is 0, so the ions moving in this direction are not affected by the Lorentz force, so the density here may be greater than the next position.

5.3 Experiment and analysis for RPA probe

Table 5.2 Parameters in experiment of RPA probe

PARAMETER	VALUE
Pressure	6.10^{-6} to 8.10^{-6} (Torr)
Probe bias voltage	-100 V
Distance between Faraday probe and engine	10 cm
Radial coordinate	0
Mass flow rate	5 sccm
RF power	50 W
Regarding voltage	0 V to 1100 V

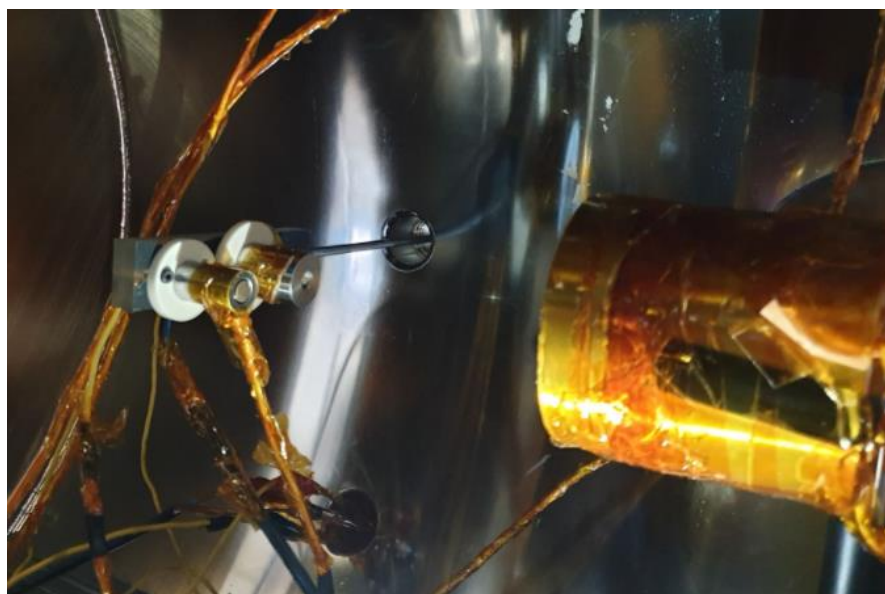


Fig. 5.10 *Experimental images in a vacuum chamber*

The I-V curve for the probe is placed 12 cm from the engine at the center. Measurements were obtained for thrusters operating at RF power is 50W, anode current rate of 5 sccm and a background pressure of about 6×10^{-6} Torr.

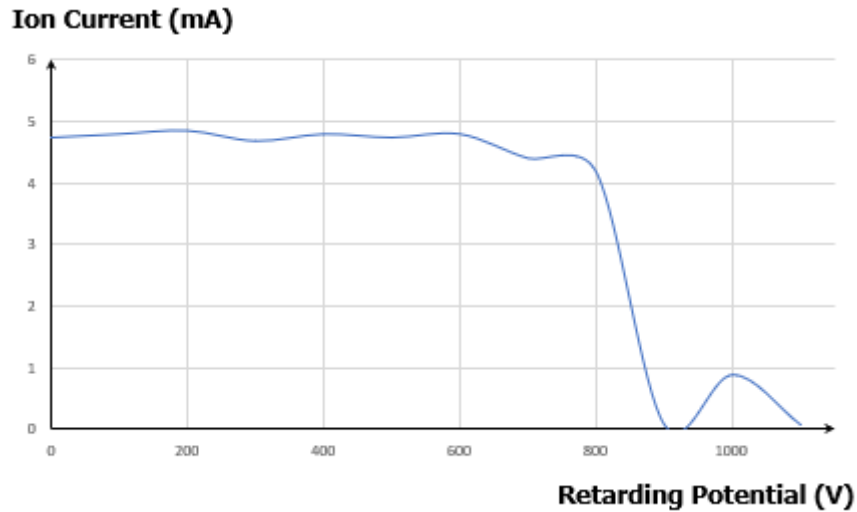
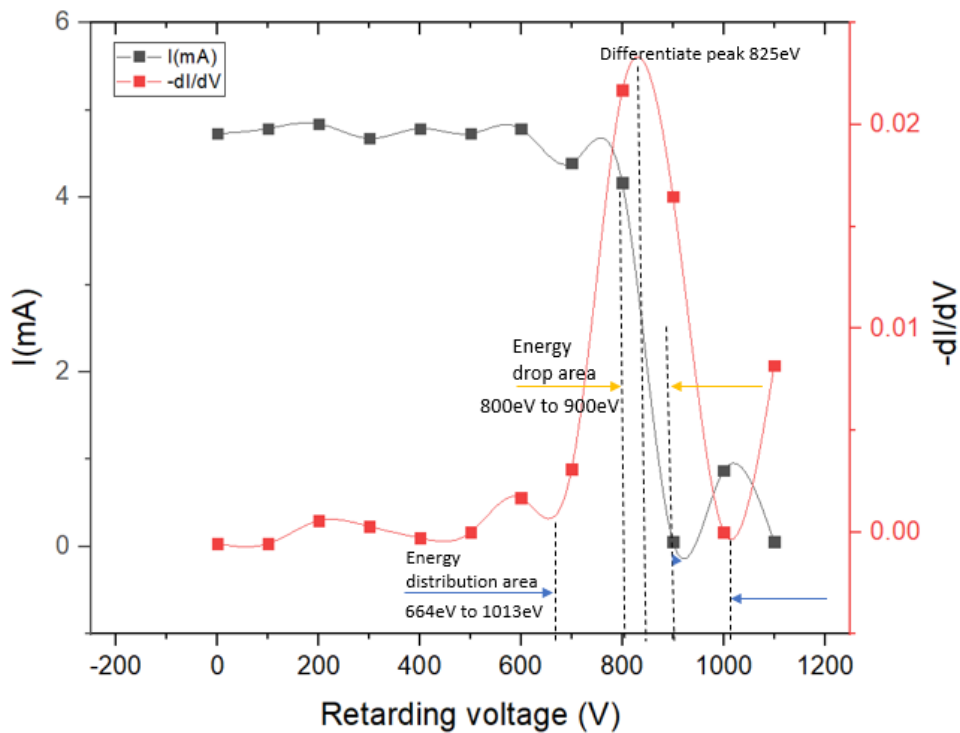


Fig. 5.11 Result experiment of RPA probe



00

Fig. 5.12 RPA I-V and dI/dV curve from measurements 100 mm at $r = 0$.

The peak in the derivative I-V characteristic is the most-probable ion potential is 825 V. If we take the normal plasma potential of about 9 V and ion thruster's acceleration voltage when testing is 1100V, we have the thruster's acceleration energy efficiency is 74%.

5.4 Calibration of Torsional Thrust Stand

Experiment system include LDS measures displacement caused by weights. Magnetic damper described a piece of copper is mounted on the Torsional Thrust Stand's swing arm; the two sides are attached with two magnets to create eddy currents (Eddy currents) in motion. This creates a force to reduce the fluctuation [46]. Force is estimated by the tilt angle for a given weight such as:

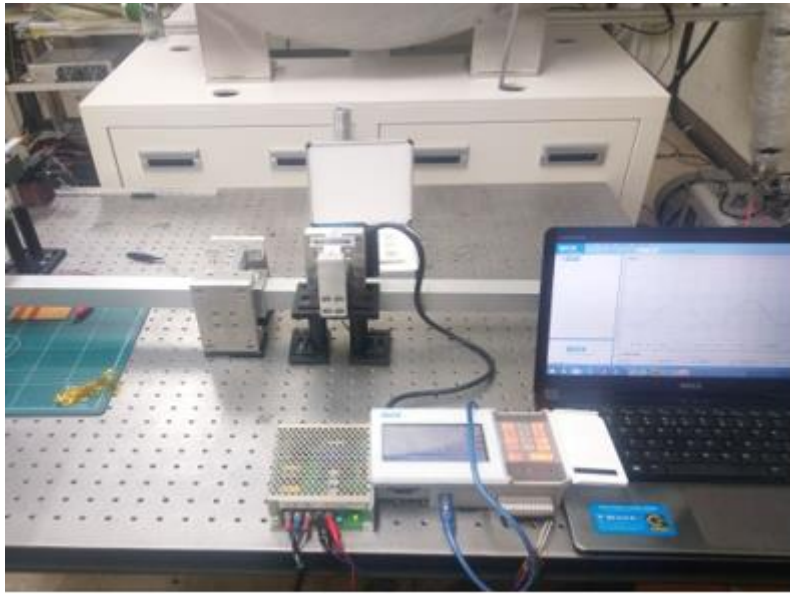


Fig. 5.13 *Experiment Torsional Thrust Stand*

$$\Delta x = |x_1 - x_2| = L_s \tan \theta \quad (5.2)$$

$$\theta = \frac{M}{k_\theta} = \frac{mgL_w}{k_\theta} \quad (5.3)$$

Where L_s is distance from center to sensor, L_w is distance from center to weight. Fig. 5.14 is a graph showing the theoretical calculated values and experimental results. As can be seen from the iconic equation, the measured value increases linearly with the input current. It was confirmed that force measurement is possible at sub mN level with the manufactured electromagnetic coil type thrust generator.

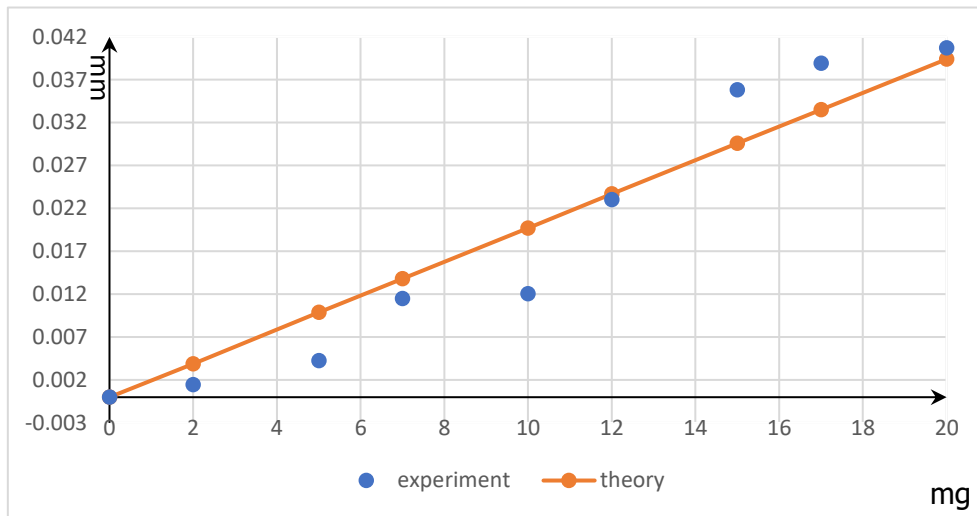


Fig. 5.14 Compare displacement measurement

5.5 Calibration of DC-powered Electrostatic Fin

For calibration DC-powered Electrostatic Fin we use a micro balance. When the voltage applied to the Fin changes the value of the displayed weight so we can find value of force between 2 Fins. It is a principle of generating a force by a potential difference applied between the two groups by composing two or more thin pins into two bail groups. The force generated at this time is theoretically calculated by the following equation:

$$F = 2n_{\varepsilon_0} V^2 \left[2,2464 - \frac{c + g}{\pi x_0} \right] \quad (5.4)$$



Fig. 5.15 *Experiment DC- Electrostatic Fin*

Fig 5.16 is showing the value of the load measured using the thrust measurement device. This result is the result of the experiment under normal pressure, and it is a load measurement test against torsional motion, so it is judged that there will be no significant difference in the experiment under vacuum. As shown in the graph, the experimental results show a similar trend to the values calculated by the above theoretical formula. As the potential difference increases from 100 V to 2000 V for the pin arrangement used. It was confirmed that the magnitude of the generated force increased from 12.3 nN to 7 mN. In the case of the electric pin type, the number and size of the pins are limited, so the magnitude of the force is mainly determined by controlling the voltage.

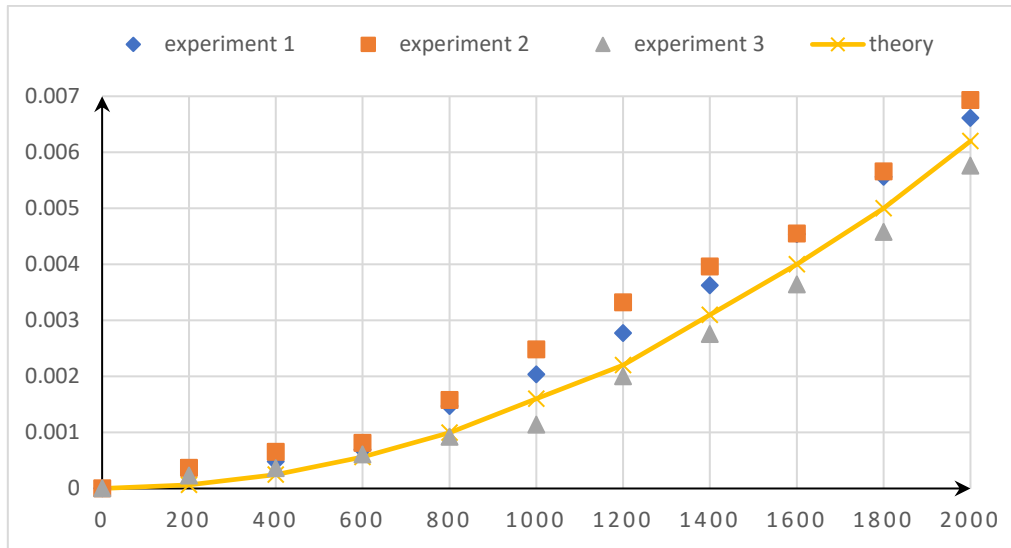


Fig. 5.16 Comparison of force measurement

In the case of a tens watt class ion thruster, considering that the thrust is at the level of 1 mN, it can be seen that the gong electric pin type thrust measuring device is at the level that can be used.

5.6 Summary

Research has shown that the engine shell (made of metal) increases the divergence angle of the ion beam. This effect is greater if the angle of divergence produced is smaller so to minimize this effect we propose to fabricate engine cover part close to grid with molybdenum ceramic or alumina ceramic. In addition, when determining the divergence angle by Faraday probe the morphology of the ion beam tended to differ from that of the ion beam produced by the engines in other studies. This is caused because the axis of the RF coil deviates from the axis of the discharge chamber by an angle of 13.24. Although there are no exact studies on the effects of this phenomenon, it can be surmised that this could reduce engine thrust or change the angle of thrust. So to solve this situation we propose a fixed holder for RF wire. Although the research is limited to experimental and experimental model with Argon propellant, it can be applied to other engine design. Experimental testing on RPA probe has been carried out, but the number

of times of testing is limited, so in the future the test will be continued to measure at different positions. Calibration for DC-powered Electrostatic Fin have been done. It was confirmed that the magnitude of the generated force increased from 12.3 nN to 7 mN

Chapter 6. Conclusion and Future Work

6.1 Conclusion

The efficiency of the RF ion thrusters is fundamentally divided according to the characteristics of the RF vibration isolators. Therefore, to analyze the efficiency of the RF ion thrusters, we are developing a theoretical analysis tool based on the RF discharge analysis. In the last year the level of usable code development was completed, and this year the theoretical benefit tool was developed based on the GUI to make it more intuitive and convenient to use. The calculated results obtained from our improved analytical model have been compared with the experimental results for both the RF ion thrusters ESA-XX with a diameter of 26 cm and the RIM-4 with a diameter of 4 cm.

This thesis also includes measuring system development such as Faraday probe, RPA probe, Torsional Thrust Stand. The Faraday Probe System comprising the Faraday cup head and the travel system was developed and completed. Several measurement results when changing the position of the Faraday cup probe and RF power and mass flow rate were collected. In addition, when determining the divergence angle by Faraday probe the morphology of the ion beam tended to differ from that of the ion beam produced by the engines in other studies. This is caused because the axis of the RF coil deviates from the axis of the discharge chamber by an angle of 13.24. Although there are no exact studies on the effects of this phenomenon, it can be surmised that this could reduce engine thrust or change the angle of thrust. So, to solve this situation we propose a fixed holder for RF wire. Although the research is limited to experimental and experimental model with Argon propellant, it can be applied to other engine

design. Research has shown that the engine shell (made of metal) increases the divergence angle of the ion beam. This effect is greater if the angle of divergence produced is smaller so to minimize this effect, we propose to fabricate engine cover part close to mesh with molybdenum ceramic or alumina ceramic. RPA Probe system is designed and developed at ARRL lab. The system is tested in a vacuum chamber at a pressure of approximately 6×10^{-6} Torr. The design and experiment of the Torsional Thrust Stand balance capable of nano-Newton level resolution were presented. This thesis focused on the development of a noncontact electromagnetic calibration technique. The experimental results also show that there is not much difference from theoretical calculation and can be fully applied to measure the force for iU-50 thrust.

6.2 Future work

The further works may include the following:

- Development and manufacture travel system 3 axis for RPA probe and Faraday probe
- Experiment of Torsional Thrust Stand in vacuum chamber.

REFERENCES

- [1] Choueiri, E. Y., "A Critical History of Electric Propulsion: The First 50 Years (1906-1956)", Journal of Propulsion and Power, Vol. 20, No. 2, 2004, pp. 193-203.
- [2] Mazouffre, S., "Electric propulsion for satellites and spacecraft: established technologies and novel approaches", Plasma Sources Science and Technology, 25(3), 2016, p.033002.
- [3] D. M. Goebel and I. Katz, "Fundamentals of Electric Propulsion", John Wiley & Sons, Hoboken, Nj, 2008.

- [4] Daniłko, Dariusz,” Overview of electric propulsion. Photonics Applications in Astronomy, Communications”, Industry, and High-Energy Physics Experiments 2014 (2014).
- [5] Roger M. Myers,” Electromagnetic Propulsion for Spacecraft. Presented in the 1993 Aerospace Design Conference”, Irvine, CA, USA, 1993, AIAA-93-1086.
- [6] Roger M. Myers, Steven R. Oelson, Melissa McGuire, Nicole J. Meckel and Joseph R. Cassady, “Pulsed Plasma Thruster Technology for Small Satellite Missions”, 9th AIAA/Utah State University Conference on Small Satellites, 1995.
- [7] Michael and J. Mitrich,” Resistojet Propulsion for Large Spacecraft Systems”, in the 16th International Electric Propulsion Conference (IEPC), New Orleans, LA, Russia, 1982.
- [8] R. G. Jahn and E.Y. Choueiri,” Electric Propulsion, Encyclopedia of Physical Science and Technology”, 3rd Ed., Vol. 5, New York, Academic Press, 2002.
- [9] Martinez-Sanchez, M. and Pollard, J. E., "Spacecraft Electric Propulsion-An Overview", Journal of Propulsion and Power, Vol. 14, No. 5, 1998, pp. 688-699.
- [10] Rafael, R Myers Consulting, ... al, “The Technological and Commercial Expansion of Electric Propulsion in the Past 24 Years”, the 35 th International Electric Propulsion Conference Georgia Institute of Technology, Atlanta, Georgia -USA, October 8 – 12, 2017.
- [11] R. Rhoads Stephenson,”Electric Propulsion Development and Application in the United States”, the 24th International Electric Propulsion Conference (IEPC), Moscow, Russia, 1995, IEPC-95-01.
- [12] J. R. Wertz and W. J. Larson, eds., “Space Mission Analysis and Design”, Torrance, California: Microcosm Press, 1999.

- [13] D. M. Goebel, Fellow, “Analytical Discharge Model for RF Ion Thrusters”, IEEE Trans. Plasma Sci. 36, 2111 (2008).
- [14] Seiji Samukawa et al, “The 2012 Plasma Roadmap”, J. Phys. D: Appl. Phys, Vol 45, No. 25, 2012.
- [15] Pham Tran Dang Quang,” Design of a rf ion thruster”, thesis 2019, University of Ulsan.
- [16] J. M. File, M. Martinez-Sanchez, and J. Szabo, “A two-dimensional hybrid model of the Hall thruster discharge “, Proc. 33rd Joint Propulsion Conf. 1997, p. 3052.
- [17] J. P. Bugeat and C. Koppel, “Fully Kinetic Hall Thruster Modeling”, Proc. 24th IEPC, 1995, p. 286.
- [18] N. Gascon, M. Dudeck, and S. Barral,” Wall material effects in stationary plasma thrusters. I. Parametric studies of an SPT-100”, Phys. Plasma. 10, 4123 (2003).
- [19] M. Dobkevicius and D. Feili, “Multiphysics Model for Radio-Frequency Gridded Ion Thruster Performance”, J. Propul. Power. 33, 939 (2017).
- [20] P. Clausing, “The Flow of Highly Rarefied Gases through Tubes of Arbitrary Length”, J. Vac. Sci. Technol. 8, 636 (1971).
- [21] Stepan V. Kaneva , Sergey A. Khartova , Vladislav V. Nigmatzyanova,” Analytical Model of Radio-Frequency Ion Thruster”, 6th Russian-German Conference on Electric Propulsion and Their Application.
- [22] D. M. Goebel, R. E. Wirz, and I. Katz, “Analytical ion thruster discharge performance model,” J. Propuls. Power, vol. 23, no. 5, pp. 1055–1067, Sep. 2007.
- [23] D. Bohm, “The Characteristics of Electric Discharges in Magnetic Fields”, A. Guthrie and R. Wakerling, Eds. New York: McGraw-Hill, 1949, pp. 1-763.

- [24] Bassner, H., Bond, A. R., Thompson, K. V., & Groh, K., “The ESA XX ion thruster”, Second European Spacecraft Propulsion Conference, Proceedings of the conference held 27-29 May 1997 in Noordwijk, the Netherlands. Edited by Michael Perry. ESA SP-398. Paris: European Space Agency, 1997., p.251
- [25] Daniel L. Brown, Mitchell L. R. Walker, James Szabo, etc. , ” Recommended Practice for Use of Faraday Probes in Electric Propulsion Testing”, Journal of propulsion and power, vol 33 , no 3, May-June 2017.
- [26] Tran Cao Van,” Experimental Investigation of the Exhaust Plume of a Micro Plasma Thruster”, chapter2, 2016.
- [27] Azziz, Y., “Experimental and Theoretical Characterization of a Hall Thruster Plume, in Aeronautics and Astronautics”., Massachusetts Institute of Technology, June 2007
- [28] Hutchinson, I. H., “Principles of Plasma Diagnostics”, Cambridge University Press, Cambridge, 1987
- [29] C. Enloe and J. Shell, 1992,” Optimizing the energy resolution of planar retarding potential analyzers,” Review of Scientific Instruments, 63, pp. 1788
- [30] K. H. Cheah, K. Low, T. Quang-Vinh, and Z. Lau,” Development of an Electrostatic Calibration System for a Torsional Micronewton Thrust Stand”, IEEE Trans. Instrum. Meas. 64, 3467 (2015).
- [31] Wangsness, R. K., Wiley & Sons,” Electromagnetic Fields”,1986.
- [32] Hrbud, I., Kemp, E.G., Yan, A.H., and Gedrimas, J.G, “Review of RF Plasma Thruster”,2007

- [33] Ivana Hrbud, G. Elijah Kemp, Allen H. Yan, Jacob G. Gedrima, “Review of RF Plasma Thruster Development,” 30th International Electric Propulsion Conference, Florence, Italy, IEPC Paper no. 2007-309
- [34] Allen, H.Y., Bradley, C.A., Jacob, G.G. (2009) “Milli Newton Thrust Stand Calibration Using Electrostatic Fins”, 47th AIAA Aerospace Sciences Meeting Including the New Horizons Forum and Aerospace Exposition.
- [35] Sadiku, M. N. OUP (1995) “Elements of Electromagnetics”, Lorrian, P., Dale Corson, R., Francois Lorrain. W. H. Freeman Company (1987) Electromagnetic Fields.
- [36] <http://esgeetech.com/products/vizglow-plasma-modeling/VizGlow/> for VizGlow, Esgee Technologies (2018).
- [37] Mert Satir, FiratSik, Emre Turkoz, Murat Celik, “Design of the Retarding Potential Analyzer to be used with BURFIT-80 Ion Thruster and Validation using PIC-DSMC Code”, 7th International Conference on Recent Advances in Space Technologies (RAST), 2015.
- [38] Quang T. D. Pham and Jichul Shin, “Better Prediction of the Performance of a Radio-frequency Ion Thruster”, Journal of the Korean Physical Society, Vol. 76, No. 2, pp. 137~144, January 2020.
- [39] Turkoz, E., Sik, F., and Celik, M, “A Study of Ion Thruster Optics through Particle Simulations and Evaluation of the Near Plume Plasma Properties”, 50th Joint Propulsion Conference, July 2014, AIAA-2014-3412
- [40] Birdsall, C. K. “Particle-in-cell charged-particle simulations, plus monte carlo collisions with neutral atoms”, pic-mcc. IEEE Transactions on plasma science 19(2), 65–85, (1991).

- [41] G. Aston, H. R. Kaufman, and P. J. Wilbu, "Ion of Two-Grid accelerator system", AIAA journal, vol. 16, no. 5, may 1978.
- [42] Zun Zhang, Haibin Tang, JunxueRen, Zhe Zhang, Joseph Wang, "Calibrating ion density profile measurements in ion thruster beam plasma", review of scientific instruments ,vol 87, no 11, 2016
- [43] Linying Chen, Renwang Song, "Faraday Cup Measurement for Beam Current in Ion Thruster", International Conference on Computational Aspects of Social Networks, 2010.
- [44] Wai-Ken Chen, "The Electrical Engineering Handbook", Pages 479-497, 2005,
- [45] <https://www.britannica.com/science/Lorentz-force>
- [46] Victor Corchete, "Eddy currents or Foucault's currents", November 2019.